# IX. PLASMA ELECTRONICS*


Prof. L. D. Smullin
Prof. H. A. Haus
Prof. A. Bers
Prof. W. D. Getty
Prof. P. Penfield, Jr.
Prof. D. J. Rose
Prof. T. H. Dupree
Prof. L. M. Lidsky
Prof. E. P. Gyftopoulos
R. R. Bartsch
W. L. Brassert
R. J. Briggs
T. S. Brown
J. F. Clarke
J. A. Davis
F. E. Dunn
P. Edmonds
M. R. Epstein
S. A. Evans
T. J. Fessenden
E. T. Gerry
J. N. Hamawi
R. Hancox
B. A. Hartenbaum
C. F. G. Hsi
H. Y. Hsieh
G. I. Kachen, Jr.
C. A. Kapetanakos
B. Kusse
S. H. Kyong
M. A. Lieberman
J. D. Mills
D. L. Morse
R. T. Nowak
A. A. Offenberger
K. C. Papadopoulos
R. R. Parker
L. M. Petrie, Jr.
S. Puri
C. G. Robertson
J. A. Ross
H. M. Schneider
P. S. Spangler
C. C. Stewart
G. Theodoridis
E. Thompson
M. T. Vlaardingerbroek
C. E. Wagner
H. L. Witting
J. C. Woo


## A. BEAM-PLASMA DISCHARGES

### 1. THE KITZELTRON

From our beam-plasma discharge experiments we have discovered the following important characteristics:

(i) Nearly 100 per cent ionization. When we fire a 10-kv, 10-amp electron beam into a hydrogen atmosphere $2 \times 10^{-5}$ torr ($\sim 6 \times 10^{11}$ mol/cc) a plasma density of approximately $10^{13}$/cc is created. This indicates that most of the gas has been pumped into, and ionized in the central column of plasma.

(ii) Good stability. A broad range of conditions can be found, consistent with (i), in which the plasma appears to decay stably (by simple diffusion) after the beam turnoff. Decay-time constants of ~0.1 sec have been observed.

(iii) Strong oscillations at $\omega_{pi}$. A survey of the radiofrequency spectrum radiated by the beam-plasma discharge has shown only two relatively narrow regions of high intensity. One is near $\omega_{pe}$ and is associated with the heating of the electrons by energy acquired from the beam-induced oscillations. The other, lower frequency, region is at approximately 1/45 $\omega_{pe}$ in a hydrogen discharge, and we associate it with an ion oscillation at $\omega_{pi}$. It is still not clear if this oscillation is driven directly by the beam or by the highly non-Maxwellian distribution of the plasma electrons. In any event, it represents a mechanism for transferring energy to the ions, and thus of heating them. We are still not able to estimate the energy level that we can impart to the ions by this method. If we can reduce charge exchange by eliminating impurities and by using a


*This work was supported in part by the National Science Foundation (Grant G-24073); and in part by Purchase Order DDL BB-107 with Lincoln Laboratory, a center for research operated by Massachusetts Institute of Technology, with the support of the U. S. Air Force under Contract AF 19(628)-500.

pulsed gas feed, the energy given to the ions may turn out to be substantial.

If the last conjecture proves true, we have the makings of a device for producing thermonuclear type plasmas. In keeping with the custom of naming such devices, I have called this one Kitzeltron. The Yiddish-German prefix is descriptive of the process of "tickling" or exciting the plasma by the electron beam.

L. D. Smullin

## 2. OBSERVATION OF LONG CONFINEMENT TIMES OF HOT ELECTRON PLASMA IN SYSTEM C

We have observed long confinement times ($10^{-2}$-$10^{-1}$ sec) of high-energy (10-50 kev) electrons and strong emission of 250-kev x radiation in the beam-plasma discharge of System C. In this system, which has been described in detail previously,[1,2] a hollow electron beam of 10-15 amps at 10 kv generates the beam-plasma discharge in hydrogen gas. The discharge is confined by magnetic mirrors with typical mirror ratios of 5 to 1 and an induction of 1000 gauss at the mid-plane. Distance between mirror peaks is 26 inches. The operating pressure ranges from $2 \times 10^{-5}$ torr to $5 \times 10^{-4}$ torr, with hydrogen gas being fed continuously into the system during operation to establish the desired pressure.

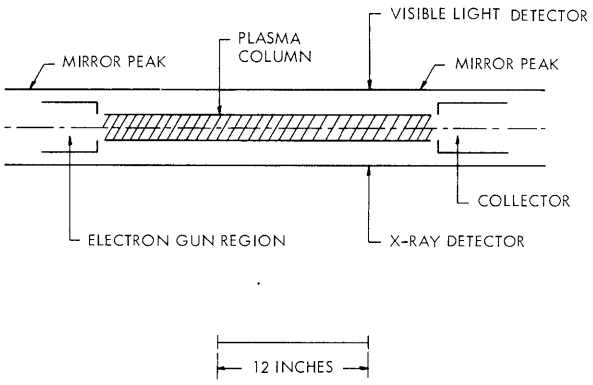


Fig. IX-1. Schematic diagram of System C showing the location of the x-ray and visible light detectors.

Plasma confinement times that range from $10^{-2}$ sec to $10^{-1}$ sec have been observed in the experiment. Confinement times in this range are predicted on the basis of loss from the magnetic bottle by electron-neutral scattering. The plasma electron density apparently decreases by two or three orders of magnitude within a few hundred microseconds after the 300-μsec beam pulse is turned off. The remaining plasma electron density, which is believed to be of the order of $10^{10}$-$10^{11}$ electrons/cm$^3$, decays slowly with a time constant as long as $10^{-1}$ sec. Measurements of the attenuation of x radiation by aluminum indicate that the x-radiation energy is at least 10 kev during the long decay. Measurements of x-ray attenuation by lead indicate that during the beam pulse the upper limit of the x-ray energy spectrum exceeds 250 kev.

The strong emission of energetic x radiation and the long confinement of hot electrons give the most dramatic evidence of the production of a hot electron plasma in

System C. Corroboratory evidence of long plasma confinement has been obtained from observation of visible light from the plasma and of wall-electrode currents. Details of our observations are described below. A schematic diagram that shows the position of our various detectors is given in Fig. IX-1.

a. X Radiation

Examples of the x-ray detector signal are shown in Fig. IX-2. The scintillation light from an NaI crystal is detected by an RCA 6199 photomultiplier. The photomultiplier output signal is passed through a transistorized DC preamplifier[3] to the oscilloscope.

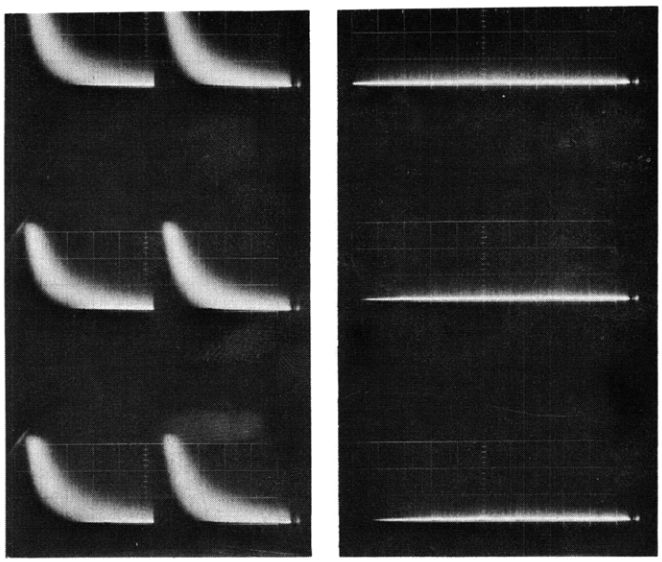


Fig. IX-2. (a) X-ray scintillation detector output for two beam pulses per trace. Sweep rate, 0.1 sec/cm; vertical calibration, 10 mv/cm. Beam voltage, 10 kv; beam cathode current, 5 amps; pressure, $2 \times 10^{-4}$ torr. (b) X-ray scintillation detector output with beam voltage off and all other conditions same as in (a).

Typical pulse heights at the oscilloscope input are 50 mv for single-photon pulses. In Fig. IX-2 the sweep rate is 100 msec per cm, and on this time scale the 300-μsec beam pulse is indiscernible. The decay of the x-ray signals that follow two beam pulses is shown in each trace of Fig. IX-2a. While the beam is on, the x-radiation flux and the maximum x-radiation energy are large and the detector output voltage is 10-100 times higher than the single-photon pulse heights that are discernible later in the afterglow. The time constant for the decay of the x-ray signal is approximately $10^{-1}$ sec for the

case shown. This is the maximum confinement time observed thus far. There is some overlap of x radiation into the next beam pulse, which occurs 0.5 sec later. The x-ray signal of Fig. IX-2a may be compared with the detector output with the beam voltage turned off as shown in Fig. IX-2b.

Attenuation of the x radiation by lead is illustrated in Fig. IX-3. The sweep rate is 0.2 msec per cm, and the voltage scale is 2 volts per cm, which is 200 times that of Fig. IX-2a. At this gain setting the x-ray detector output can be observed during the beam pulse. The preamplifier is saturated in Fig. IX-3a. The 200-fold decrease from the level of Fig. IX-3a to that of Fig. IX-2a occurs in approximately 300 μsec as

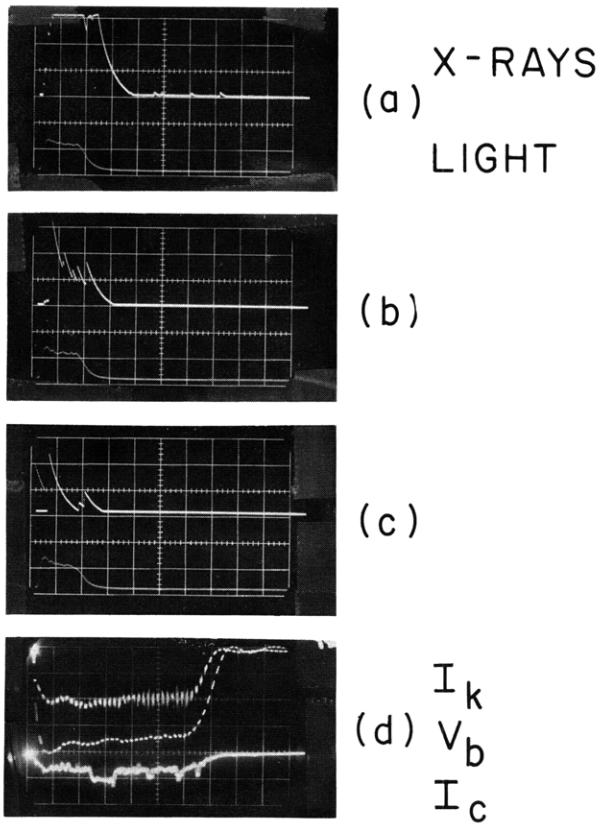


Fig. IX-3. (a) X-ray detector signal and light with no lead absorber placed in front of the scintillator. Sweep rate, 0.2 msec/cm; vertical calibrations, 2 volts/cm for the x-rays and 5 volts/cm for the light. (b) With 1/32 inch of lead. (c) With 1/16 inch of lead. (d) $V_b$, 3600 volts/cm; $I_k$ and $I_c$, 5 amps/cm; sweep rate, 50 μsec/cm.

shown by both the light and x-ray signal decay in Fig. IX-3. The curves in Fig. IX-3a, 3b, and 3c are taken for increasing thicknesses of lead sheet that is placed in front of the

scintillator. Passage through thicknesses of lead of approximately 1/16 inch indicates a maximum x-ray energy exceeding 250 kev.

Figure IX-3d illustrates the time variation of $V_b$, the beam voltage; $I_k$, the gun cathode current; and $I_c$, the collector current. The examples shown here are for the conditions of Fig. IX-3a, 3b, and 3c.

Attentuation of the x radiation as it passes through aluminum was measured quantitatively with the aid of a 256-channel pulse-height analyzer. The number of counts per channel was plotted as a function of aluminum absorber thickness to determine an absorption coefficient and consequently the x-ray energy. The pulse-height analyzer had a minimum dead time of 10 μsec and therefore could accept no more than 30 counts within a 300-μsec beam pulse. The x-ray count is therefore essentially averaged over the afterglow, which lasted for several hundred milliseconds. These measurements indicate that the x-ray energy ranges up to 50 kev. Our conclusion is that the maximum x-ray energy is several times larger during the beam pulse than during the afterglow.

b. Visible Light

Several oscilloscope traces of the total visible light that is detected by a 6199 photomultiplier are shown in Fig. IX-4. The sweep rate in this figure is 20 msec per cm. The time variation of the total light during the beam pulse can be seen on a much less sensitive scale in Fig. IX-3a, 3b, and 3c. The light decreases by a factor of approximately $10^3$ in the first 200 μsec after the beam pulse. After this relatively rapid decrease of intensity the light decays slowly for the next 30-40 msec, as shown in

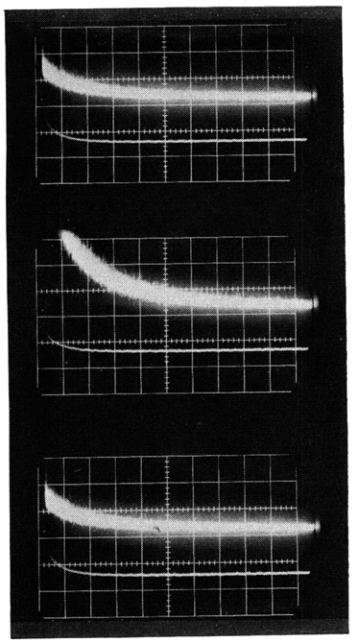


Fig. IX-4. Three examples of x-ray and visible light decay. Sweep rate, 20 msec/cm. Vertical calibrations are 20 mv/cm for the x-rays and 5 mv/cm for the light.

Fig. IX-4. The decay time constants for the light are of the same order of magnitude as for the x radiation. In general, the light appears to decay slightly faster.

From previous work[1,2] it is known that strong RF radiation at 40 Gc/sec is produced by the beam-plasma discharge in System C. If it is assumed that this radiation is at the electron plasma frequency, then the corresponding plasma density is $2 \times 10^{13}$ electrons/cm$^3$. Considering that immediately after the beam pulse the light intensity decreases by 2-3 orders of magnitude, we believe that the electron density decreases by the same factor and is, therefore, in the range $10^{10}$-$10^{11}$ electrons/cm$^3$ at the beginning of the long plasma decay.

W. D. Getty, L. D. Smullin

References

1. W. D. Getty and L. D. Smullin, System C: Strong interaction between a high-density, hollow electron beam and a plasma, Quarterly Progress Report No. 70, Research Laboratory of Electronics, M.I.T., July 15, 1963, pp. 114-116.

2. L. D. Smullin, System C, Quarterly Progress Report No. 71, Research Laboratory of Electronics, M.I.T., October 15, 1963, pp. 115-116.

3. Designed by T. J. Fessenden, Research Laboratory of Electronics, M.I.T., September 1963.

## 3. RADIOFREQUENCY SPECTRUM RADIATED BY BEAM-PLASMA DISCHARGE

The radiofrequency spectrum from 10 mc to 44 kmc at three sampled times during the beam-plasma discharge has been measured for three different gases. For all of the experiments reported here, the following parameters were kept constant, and were checked from time to time as the spectrum was plotted.

| | |
|---|---|
| Magnetic mirror: | 3 to 1 |
| Central magnetic field: | 280 gauss |
| Beam voltage: | 6 kv |
| Beam perveance: | 1 microperv |
| $T_b$ (denotes duration of regime 1): | 4-6 μsec[1] |
| Beam pulse: | 170 μsec |
| Repetition rate: | 30 pulses per second |
| Pressure: | 1.1 μ Hg Hydrogen |
| | 2.8 μ Hg Helium |
| | 0.25 μ Hg Argon |

Figure IX-5 shows the location of the RF detectors that were used to obtain the frequency spectrum. Figure IX-6 shows the schematic diagram of the measuring instruments.

In order to obtain a large dynamic range, the gain of the SPA-4a receiver is usually

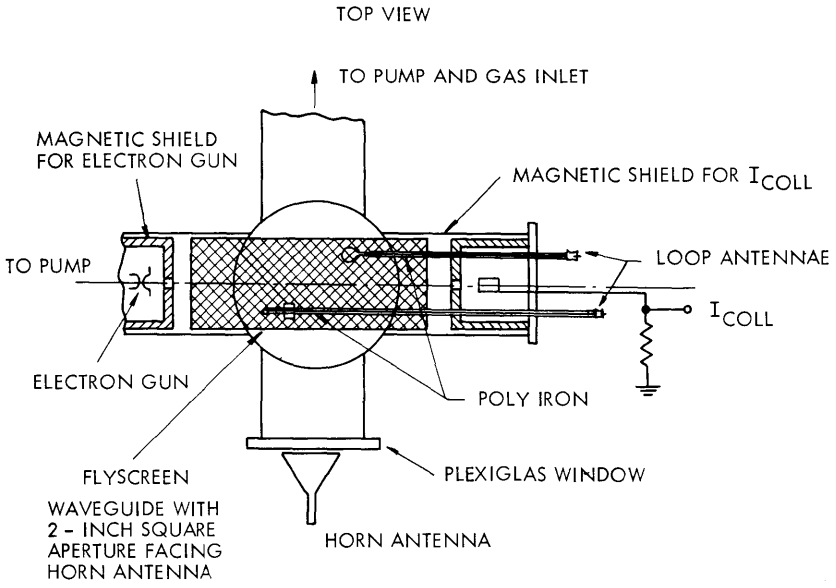


Fig. IX-5. Diagram showing the location of RF detectors in System A. Helmholtz coils are not shown.

set high. The pulse-shaping network eliminates any overshoot caused by large spikes of RF radiation.[2] The boxcar integrator could be adjusted to sample the synchroscope output of the SPA-4a spectrum analyzer at appropriate times. Various frequency filters were used to sort out the spectrum, since the receiver can respond to a given frequency at several dial settings. No amplitude calibration of the receiver has been made. Thus, we cannot compare amplitudes at different frequencies. For a fixed gain setting, however, we can compare amplitudes at any one frequency for different time delays.

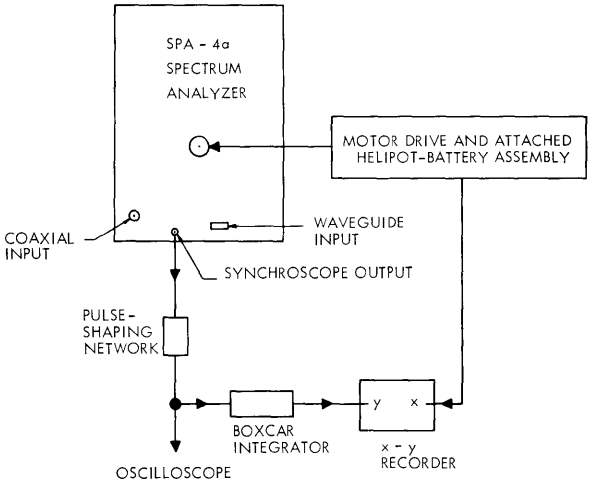


Fig. IX-6. Schematic diagram of the measuring instruments.

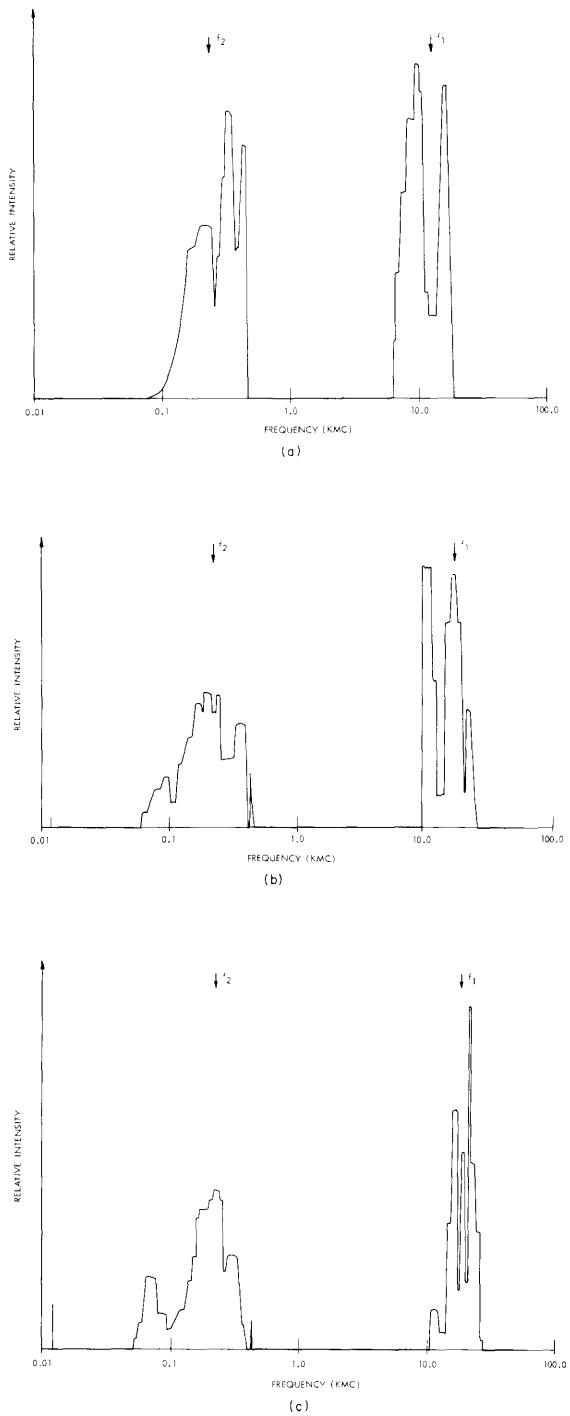


Fig. IX-7. R-F spectrum of the beam-plasma discharge in helium: (a) 15 μsec after $T_b$; (b) 75 μsec after $T_b$; and (c) 145 μsec after $T_b$. The relative intensities are meaningful only within narrow bands. Intensities of the two bands cannot be compared.

Each sweep of a band of frequencies represents an average plot of 3-70 pulses per 10 mc. The number of pulses per 10 mc depends on the range selected by the SPA-4a receiver. A frequency spectrum at a particular sampled time such as the one shown in Fig. IX-7a represents the power emitted by approximately 200,000 different pulses. This spectrum may be interpreted as the probability of seeing a particular frequency emitted during the sampled time interval of one typical pulse of the beam-plasma discharge.

Figure IX-7 shows the frequency spectrum for a 10-μsec interval during the beam-plasma discharge in helium gas at 15 μsec, 75 μsec, and 145 μsec after the beginning of regime 2.[1] Generally, for the nine experimental conditions, the spectrum shows principally two large bands of oscillations. Typically, one band extends from 10 kmc to 27 kmc, and the second band, its width varying with the gas, extends from 30 mc to 500 mc. If one takes the center of the first band, $f_1$, and compares it with the center of the second band, $f_2$, one finds ratios of (see Fig. IX-7) approximately 50 for hydrogen, 80 for helium, and 200 for argon. If one assumes that the ions in these plasmas are singly ionized, then the ratios of $\omega_{p-}/\omega_{p+}$ are 43 for hydrogen atoms, 61 for hydrogen molecules, 86 for helium, and 272 for argon.

H. Y. Hsieh

References

1. L. D. Smullin, B. A. Hartenbaum, and H. Y. Hsieh, Electron beam-plasma interaction experiments, Quarterly Progress Report No. 67, Research Laboratory of Electronics, M.I.T., October 15, 1962, pp. 71-76.

2. H. Y. Hsieh, System A: Radiofrequency signals radiated by beam-plasma discharge, Quarterly Progress Report No. 72, Research Laboratory of Electronics, M.I.T., January 15, 1964, pp. 117-121.

## 4. ROTATIONAL INSTABILITY IN THE BEAM-PLASMA DISCHARGE

The existence of an instability that transports plasma across the magnetic field in the beam-plasma discharge[1] has led to speculation about some plasma properties and loss mechanisms. The direction of rotation of the observed instability suggests that the plasma electrons have energies of several hundred volts while the ions have average energies of only a few volts. The condition for triggering the instability indicates an optimum pressure for obtaining a hot discharge.

### a. Discharge Core

The rotation of a spoke of plasma in the right-hand sense about the magnetic field implies the existence of an inward-directed electric field. The conditions under which the plasma can attain a negative potential with respect to the walls of the discharge

chamber are examined. The criterion for determining the sign of the plasma potential is as follows: If we neglect space charge and the loss rate of ions exceeds the loss rate of electrons, the plasma will attain a negative potential when space charge is considered. We shall direct our attention only toward obtaining the potential of the core or source region of the plasma. Perpendicular diffusion will be neglected, since it is clear that the inclusion of perpendicular diffusion can only drive the plasma more negative. Velocity distribution effects will be neglected. The assumption of no perpendicular diffusion will tend to be balanced by the high loss rate of low-energy electrons from the magnetic mirror. All gradients of temperature and density are neglected. These assumptions lead to a one-dimensional model of scattering in a magnetic mirror.

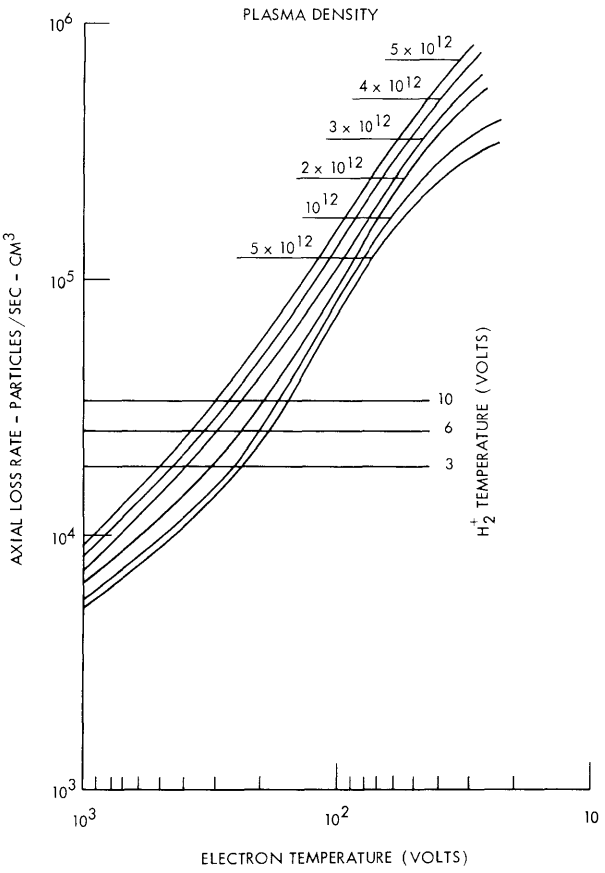


Fig. IX-8. Axial loss rates from the magnetic mirror. $H_2$ density, $10^{13}/cm^3$.

The rate at which particles are scattered out of a magnetic mirror is the rate at which particles are scattered through 90° multiplied by the probability of being scattered into the loss cone. Electron scattering is governed by e-e, e-i, and e-n collisions. The Coulomb collision time is taken to be Chandrasekhar's deflection time.[2] The neutral collision time is given by Brown[3] for electrons of energy less than 100 volts. For electron energies above 200 volts the cross section for large-angle (momentum transfer) deflection was obtained by the numerical integration of the elastic differential cross section given by Moiseiwitsch and Williams[4] and the inelastic differential cross section given by Marton and Schiff and by Morse.[5]

It is assumed that the collision cross section for e-$H_2$ is twice that given for e-H. It is assumed that only $H_2^+$ is present, because of the low probability of formation of $H^+$ by direct electron impact with $H_2$.[6] Multiple processes cannot play an important role, because of the short time scale. A build-up of H in the continuously pumped system must be discounted because of the low duty ratio. Ion scattering is governed by i-i and i-n collisions. The total $H_2^+$-$H_2$ collision cross section is given by Simons et al.[7]

For ions of a few volts energy, the mean-free path for a 90° deflection is less than the distance between the mirrors. Thus the ion motion is "collision dominated." The maximum rate of escape of the ions is given by the rate of effusion from the ends of the magnetic mirror.

The loss rates of electrons and ions for given electron and ion temperatures and plasma densities are plotted in Fig. IX-8. The plot indicates that for a plasma consisting of electrons that have an average energy above several hundred volts and ions that have an energy of approximately 5-10 volts the plasma potential will be negative.

b. Rotating Instability

It will be assumed that with some modifications Simon's theory of cross-field instability[8] is a fair explanation of the instability observed in the beam-plasma discharge. By combining the results of theory and experiment, it is possible to predict the variation of electron temperature with pressure. It will be seen that there is an optimum pressure for producing a hot discharge. Simon's theory is modified in two ways. First, the wave number that is parallel to the magnetic field ($k_{||}$) is set equal to zero. Axial loss is reintroduced by considering scattering out of the magnetic mirror. Second, the effect of ionizing collisions is included. If each unit length of discharge is assumed to contribute the same amount of scattering loss, the continuity equation becomes

$$\frac{\partial n}{\partial t} = -\nabla \cdot \Gamma - (\nu_s - \nu_i)n,$$

where $\nu_s$ is the scattering loss rate and $\nu_i$ is the ionization rate. The effective axial loss rate, $\nu_s - \nu_i$, could be calculated if the electron energy distribution function were known. The distribution function is not known, however, and $\nu_s - \nu_i$ cannot be calculated directly. We are forced to make an approximation. We shall formulate a model for the plasma that is external to the core of the plasma, which, when combined with experimental information, will yield the effective loss rate.

The plasma that is external to the discharge core is described by equations that are different from those used to describe the source region. The loss of electrons is assumed to be controlled by perpendicular diffusion and parallel scattering out of the magnetic mirrors. That the perpendicular diffusion is caused by neutral collisions rather than by Coulomb collisions is suggested by the observed exponential decay of plasma density with increasing radius. The action of the perpendicular electric field on the electrons is negligible compared with the action of the parallel electric field, because of the very small perpendicular electron mobility. But the effect of the parallel electric field is felt only through the alteration of the electron loss cone, which is proportional to $T_+/T_-$, which is also supposed to be small. Thus, to a good approximation the electron flow is independent of the space-charge fields. The ion flow is not

so simple because the electric field constrains the ions both in the parallel and perpendicular directions. The plasma density is given by

$$\frac{\partial n}{\partial t} = D_{\perp_-} \frac{\partial^2 n}{\partial x^2} - (\nu_s - \nu_i)n. \tag{1}$$

In the steady state we have

$$\nu_s - \nu_i = \frac{D_{\perp_-}}{L_o^2}.$$

The characteristic length of the density gradient, which is taken from the experiment, yields $\ell/L_o = 10$. Setting $k_{||} = 0$ and taking $\ell/L = 10$ require the assumption that sheaths will match the plasma potential to the wall and prevent the perpendicular electric field from becoming very large there.

The frequency of rotation of the instability is given by

$$\omega_R = k_\perp \left[ \frac{E_o}{B} \left( 1 + \frac{1}{2L_o^2\Lambda^2} \right) - \frac{T_+}{L_o B} \left( 1 - \frac{(\omega\tau)_+}{(\omega\tau)_-} \frac{T_-}{T_+} \right) \right]. \tag{2}$$

The growth rate is given by

$$\omega_I = -\left( \Lambda^2 + \frac{1}{L_o^2} \right) \mu_{\perp_-} T_- + \frac{k_\perp^2}{L_o \Lambda^2 (\omega\tau)_+ B} \left\{ E_o \left[ 1 + \frac{1}{2L_o^2\Lambda^2} \right] - \frac{T_+}{L_o} \left[ 1 - \frac{(\omega\tau)_+}{(\omega\tau)_-} \frac{T_-}{T_+} \right] \right\} \tag{3}$$

where

$$\frac{1}{L_o} \equiv \frac{1}{n_o} \frac{\overline{dn_o}}{dx}$$

$$k \equiv \pi/\ell$$

$$E_o = -V/\ell$$

$$\Lambda^2 = 2(\pi/\ell)^2$$

$\ell$ = distance between plasma core and discharge chamber wall.

The real part of $\omega$ may be substituted in the expression for the imaginary part of $\omega$, thereby yielding

$$\omega_I = -\left( 1 + \frac{1}{L_o^2\Lambda^2} \right) \frac{T_-}{(\omega\tau)_- B} + \frac{k_\perp \omega_R}{L_o \Lambda^2 (\omega\tau)_+}. \tag{4}$$

The condition for marginal stability ($\omega_I=0$) gives a relationship between the electron temperature and $\omega_R B$.

$$T_- = k_\perp \frac{(\omega\tau)_-}{(\omega\tau)_+} \frac{1}{L_o\Lambda^2\left(1 + \frac{1}{L_o\Lambda^2}\right)} (\omega_R B) \tag{5}$$

The electron temperature as a function of pressure still has not been measured, but $\omega_R B$ at the onset of instability has been measured. Let us use the theory of cross-field

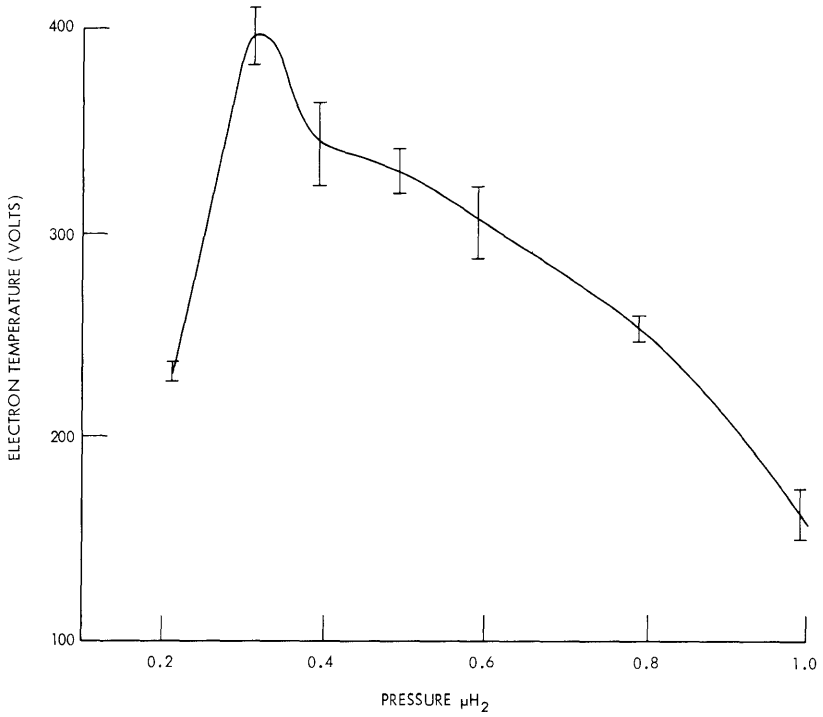


Fig. IX-9. Electron temperature vs pressure at the onset of rotating instability.

instability to estimate the behavior of the electron temperature with pressure. Equation 5, with the experimentally determined values of $\omega_R B$ used, is plotted in Fig. IX-9. The variation of $T_-$ with p agrees qualitatively with observation of the variation of the strength of x-ray production at different pressures.

B. A. Hartenbaum

## References

1. B. A. Hartenbaum, Beam-plasma discharges. System B: Rotational instability in the beam-plasma discharge, Quarterly Progress Report No. 72, Research Laboratory of Electronics, M. I. T., January 15, 1964, pp. 121-124.

2. L. Spitzer, Physics of Fully Ionized Gases (Interscience Publishers, Inc., New York, 1956), p. 77.

3. S. C. Brown, Basic Data of Plasma Physics (The Technology Press of Massachusetts Institute of Technology, Cambridge, Mass., and John Wiley and Sons, Inc., New York, 1959), p. 5.

4. B. L. Moiseiwitsch and A. Williams, The elastic scattering of fast electrons and positrons by hydrogen and helium atoms, Proc. Roy. Soc. (London) A250, 337 (1959).

5. Reported by H. Massey and E. Burhop, Electronic and Ionic Impact Phenomena (Oxford University Press, London, 1952), pp. 177-178.

6. H. Harrison, The Experimental Determination of Ionization Cross Sections of Gases under Electron Impact (Catholic University Press, Washington, D. C., 1956).

7. J. Simons, C. Fontana, A. Francis, and L. Unger, The low velocity scattering of $H_2^+$ in hydrogen – The determination of neutralization, J. Chem. Phys. 11, 312-316 (1943).

8. A. Simon, Instability of a partially ionized plasma in crossed electric and magnetic fields, Phys. Fluids 6, 382-388 (1963).

## B. BEAM-EXCITED ION-PLASMA OSCILLATIONS

Several changes in the apparatus[1] for the investigation of a beam-excited ion instability in a hot electron plasma have led to the observation of interaction at the ion-plasma frequency.

In the first place the magnetic mirror field, in which the cavity for the cyclotron discharge is placed, was made more symmetrical and stronger. Second, the continuous microwave power, exciting the discharge, was increased to 100 watts, and simultaneously the frequency decreased to 2.8 kmc. With these changes, the condition that the electron-cyclotron frequency must somewhere in the cavity be equal to the frequency of the input power could easily be met. At low pressures, $\sim 10^{-5}$ torr, a cyclotron discharge producing x-rays could be excited. At higher pressures the yield of x-rays goes down rapidly; but the discharge becomes brighter. (The electron-cyclotron resonance discharge is discussed in Section IX-C.)

In our earlier experiment,[1] we looked for and did not find self-excited oscillations around $\omega_{pi}$ when a beam was fired into the electron-cyclotron discharge. We concluded that even if an interaction occurred between beam and ions it was too weak to establish self-excited oscillations or to build up a measurable signal from noise. Therefore, in the next set of experiments, a grid-modulated gun was used. Approximately 2 volts rms was applied to a crude grid across the cathode, at frequencies in the range 10-200 mc. We measured the modulated beam current reaching the collector. At frequencies around 70 mc there was a pronounced enhancement of the signal when the hot electron plasma was present. Typically at the peak the RF collector current was approximately 10 times higher with the hot plasma than without it. Since the electron-plasma frequency

is in a cyclotron discharge with $\omega_p \approx \omega_{ce}$, it follows that in hydrogen the ion-plasma frequency is indeed of the order of 70 mc. The beam voltage used was near 250 volts, and the current, 10 ma. The beam diameter is estimated to be 1 mm.

Briggs and Bers[2] deduced a condition for infinite gain at the ion-plasma frequency in an unbounded beam-plasma system. Applying Allis' condition, namely $\lambda_{pb} < \lambda_D$, to our case, we find that the electron temperature of the plasma must be

$$V_{TE} > V_b \frac{n_p}{n_b} (\text{volts}),$$

where $n_p$ and $n_b$ are the particle densities of the plasma and the beam, respectively, or, by substituting the relevant numbers, $V_{TE} > 2.5$ kv. It is unlikely that this temperature would be reached in our 100-watt cyclotron discharge. On the other hand, the condition used may be too strong. It is possible that transverse waves might be responsible for the amplification observed. Transverse space-charge interaction may occur when the dielectric constant of the plasma that is perpendicular to the beam (and the external magnetic field) is negative. The zeros of this dielectric constant are given by Bers.[3] Using his notation, we can reduce the equation for the low-frequency root of $K_\perp = 0$:

$$\omega_{01}^2 = \omega_{pi}^2 \Big/ \left(1 + \omega_{pe}^2/\omega_{b_-}^2\right),$$

since $\omega_{pe}^2 \gg \omega_{b_+} \omega_{b_-}$. Since in a cyclotron discharge the electron-plasma frequency must be of the order of the cyclotron frequency of the electrons, we find that an interaction may occur in our experiment at $\omega_{pi}/\sqrt{2}$.

M. T. Vlaardingerbroek, M. A. Lieberman

## References

1. M. T. Vlaardingerbroek, M. A. Lieberman, and L. D. Smullin, Beam-excited ion-plasma oscillations, Quarterly Progress Report No. 72, Research Laboratory of Electronics, M.I.T., January 15, 1964, p. 125.

2. R. J. Briggs and A. Bers, Electron-beam interactions with ions in a warm plasma, Quarterly Progress Report No. 69, Research Laboratory of Electronics, M. I. T., April 15, 1963, p. 71.

3. W. P. Allis, S. J. Buchsbaum, and A. Bers, Waves in Anisotropic Media (The M.I.T. Press, Cambridge, Mass., 1963), p. 233.

## C. ELECTRON-CYCLOTRON RESONANCE DISCHARGE*

Since the last report by Fiocco and Smullin[1] the electron-cyclotron resonance discharge experiment has been improved through the addition of a large amount of electronic and other types of equipment. New magnet coils have been built, and it is now possible to obtain a magnetic field at the center of the magnetic mirror field of over 1000 gauss for almost indefinite periods. It was found that the machine generated large fluxes of x-rays, and consequently it was necessary to encase the resonant cavity in a sheath of 0.5-inch lead. The x-ray flux is now less than 5 mr/hr in the vicinity of the machine.

A large number of experiments of an exploratory nature has been performed, and the principal results of these experiments will be reported on here. In these experiments the discharge was produced in hydrogen by 1-μsec pulses of microwave energy at a frequency of 2800 mc. These pulses occurred 1000 times each second at a peak level of 50 kw. These pulsed experiments are complementary to the high-power, cw experiment of R. A. Dandl at Oak Ridge National Laboratory.[2]

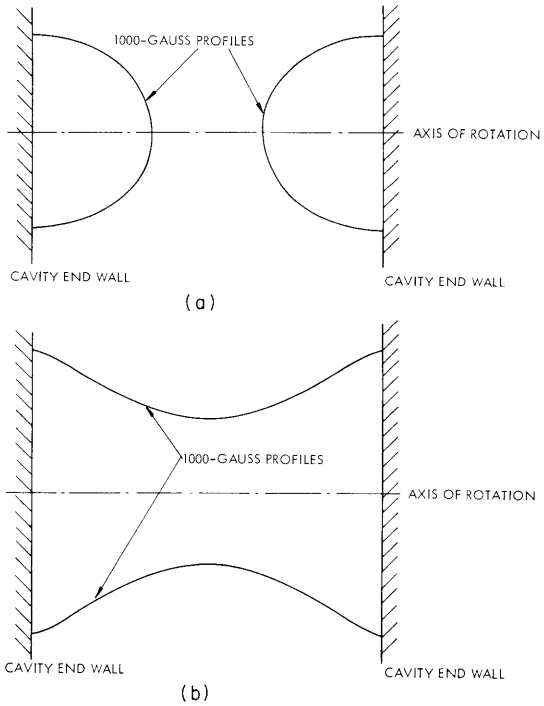


Fig. IX-10. The 1000-gauss profiles for magnet currents (a) less than 46 amps and (b) greater than 46 amps.

*This work was supported in part by the U.S. Atomic Energy Commission under Contract AT(30-1)-3221.

The steady magnetic field that is produced along the axis of the cavity is in the mirror configuration with a mirror ratio of approximately 4 inside the cavity. The magnets are capable of producing a field of more than 1000 gauss at the center of the mirror. The shapes of the surfaces representing the 1000-gauss contours within the cavity are important. It is on these surfaces that cyclotron resonance occurs, and thus they define the regions in which the plasma is heated. For low (less than 46 amps) currents in the magnets, these surfaces of revolution have the form shown in Fig. IX-10a. For magnet currents greater than 46 amps the 1000-gauss profile has the form indicated in Fig. IX-10b.

1. Operation of the System

The characteristics of the system are divided into three groups by the background pressure: the low-pressure region from the base pressure to approximately $2 \times 10^{-5}$ torr; the intermediate range, from $2 \times 10^{-5}$ torr to $2 \times 10^{-4}$ torr; and the high-pressure range from $2 \times 10^{-4}$ torr to $10^{-3}$ torr. Thus far these constitute the ranges of pressure over which the experiment has been studied.

a. Low-Pressure Region

(i) X-ray Characteristics

This region is characterized by very strong x-rays of large intensity. X-ray fluxes of over 2.5 roentgens/hour have been observed at an unshielded port in the cavity. A crude absorption measurement of these x-rays made by using aluminum indicated that their energy was approximately 250 kev. The x-ray maximum appears at a pressure of 7 or $8 \times 10^{-6}$ torr.

X-ray photographs of the discharge, obtained by using a fluorescent screen and a pinhole in the lead shielding, indicate that most of the x radiation is coming from the cavity end walls. On the photograph there was no evidence of x-rays coming from the cavity volume or cylindrical cavity walls.

Time studies of the x-rays were made by using an NaI scintillator. The scintillator indicates that nearly all of the x-rays are produced during the 1 μsec in which the microwave power is applied. At the end of the microwave pulse the x-ray intensity falls in approximately 10 μsec to a level of less than 1/1000 that of its peak. The interpulse x-ray level then decays relatively slowly with a time constant of the order of 10 msec. The x-rays emitted by the discharge between pulses of microwave energy were found to be coming from the volume of the discharge and/or from the cylindrical cavity walls.

These measurements indicate that there is a group of high-energy electrons in the discharge which, in the absence of microwave energy, is confined by the magnetic mirror for times of the order of 10 msec. During the microwave pulse these hot electrons are forced into the cavity end walls by the large microwave fields.

As a function of the magnet current, the x-rays first appear at 26 amps and increase slightly in intensity until 47 amps, whereupon they increase by a factor of approximately 3 for pressures between $5 \times 10^{-6}$ torr and $10 \times 10^{-6}$ torr.

(ii) Light

The plasma in the low-pressure region generates very little light. Its intensity is only a few times that of the background. The distinguishing characteristics of this light are (a) that it continues to build up after the microwave pulse for approximately 10 μsec and (b) that it decays very slowly with a time constant of several hundred microseconds. This time constant has not been accurately measured.

(iii) Cyclotron Radiation

In this lowest range of pressures a large amount of cyclotron radiation is observed for magnet currents greater than 45 amps when the 1000-gauss magnetic surface has the form of Fig. IX-10b. The cyclotron radiation is observed coming back through the S-band waveguide and through a TR switch placed in the waveguide. The RF envelope consists of random pulses of approximately 5-μsec duration which are observed up to 600-700 μsec after the pulse of microwave power from the magnetron. The pulses of cyclotron radiation are of very large amplitude and are large enough to saturate the crystal detector placed in the TR switch. The cyclotron radiation has not been thoroughly investigated.

(iv) Diamagnetic Signal

In this pressure region the diamagnetic signal is small until the magnetic current reaches 40-45 amps, and then it increases rapidly with the magnet current. At times it is possible to observe fluctuations in the diamagnetic signal at a frequency of 10 mc or 20 mc during the period in which strong cyclotron radiation from the discharge is observed.

b. Medium-Pressure Range

This region is announced by an abrupt increase in the light generated by the discharge with a sharp reduction in the x-ray intensity. The transition pressure is between $2 \times 10^{-5}$ torr and $3 \times 10^{-5}$ torr. The upper pressure bound of this region is marked by a further jump in the light intensity and a change in the discharge characteristics. The upper bound is much less pronounced and occurs between $2 \times 10^{-4}$ torr and $3 \times 10^{-4}$ torr.

The lower transition is the most interesting. At the transition point all of the dependent parameters of the system fluctuate wildly: the light, the x-rays, the diamagnetic signal, even the neutral-gas pressure (as indicated by an ionization gauge). It is believed that the regime of operation of the system is constantly changing from that of the low-

pressure range to that of the intermediate range. The frequency of the fluctuations is slow and is a few per second.

A tentative explanation for these observations is as follows. At the transition pressure the initial operation of the system is that characterized by the lower pressure; the x-ray intensity is high, with little light and strong electromagnetic fields in the interior of the discharge. In this type of operation the discharge "pumps" and the particle density inside the discharge increases with a corresponding decrease in pressure in the region of the ion gauge. The influx of particles into the discharge, however, has the effect of cooling the discharge in several ways: first, there are more neutrals to be ionized; second, the electron, and hence the ion density, increases rapidly, and hence the energy transfers by electron-electron and then electron-ion collisions rapidly cool the very hot electrons that were produced earlier; and third, the higher electron density shields the applied microwave field from this region of the discharge and less energy is available for further ionization. By these processes the discharge collapses – much fewer x-rays are produced as the electron gas cools, the light output increases with the electron density, the diamagnetic signal decreases, and, finally, there is a large outflux of particles from the discharge. These particles are then pumped away by the pumps and the process is repeated.

(i) Light

Figure IX-11 is a graph of the light produced by the discharge as a function of the background gas pressure. These curves represent a 5-μsec integration of the light during the peak of the light pulse (approximately 5 μsec after the end of the magnetron pulse). The violent fluctuations of the light in the 50-, 60-, and 70-amp curves at $3 \times 10^{-5}$ torr are due to the previously described process and to the inability of the x-y recorder to follow the fluctuations of the signals. The near linearity of the curves suggests that the electron density is relatively independent of neutral density over this whole range.

As a function of the magnetic field, the light has two maxima as shown in Fig. IX-12. At the first maximum, which occurs at 26 amps, the 1000-gauss points on the axis are at distances of $1.25\ \lambda/4$ from the left wall and $1.5\ \lambda/4$ from the right wall of the cavity. Here, $\lambda$ is the free-space wavelength of the microwave energy. There is some question as to the accuracy of the distance measurements, and it is believed that this first maximum may occur because the 1000-gauss profile coincides with the first local maximum of the microwave electric fields within the cavity. These maxima would be expected to appear at $\lambda/4$ from each of the cavity walls. The second maximum of the light occurs just at the point at which the 1000-gauss profile passes through the center of the magnetic mirror. Therefore, this is the transition point between the two types of 1000-gauss profiles illustrated in Fig. IX-10.

The shape of the light pulse in the intermediate-pressure regime is similar to its

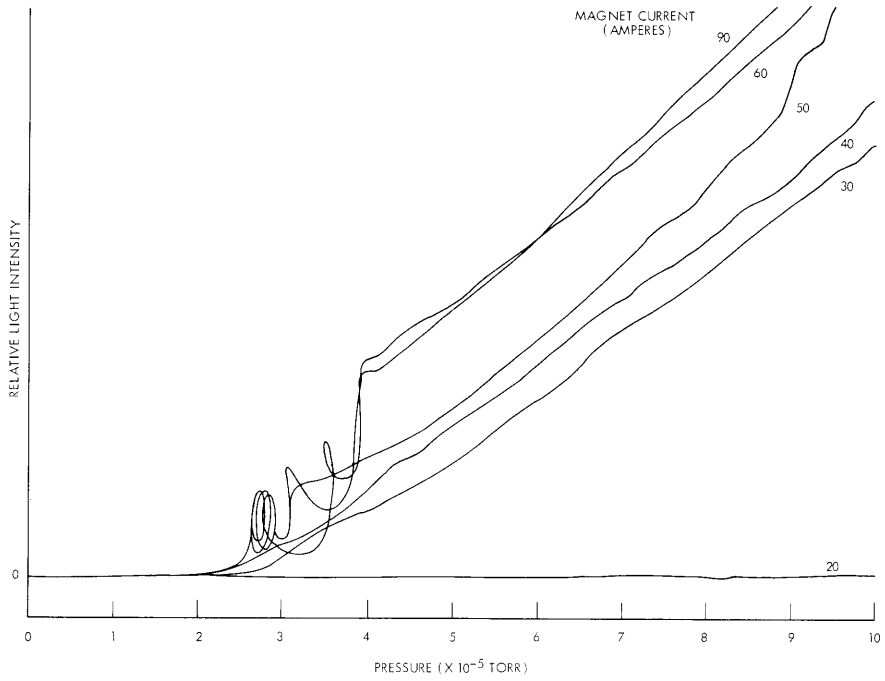


Fig. IX-11. Relative light intensity as a function of pressure for various magnetic fields.

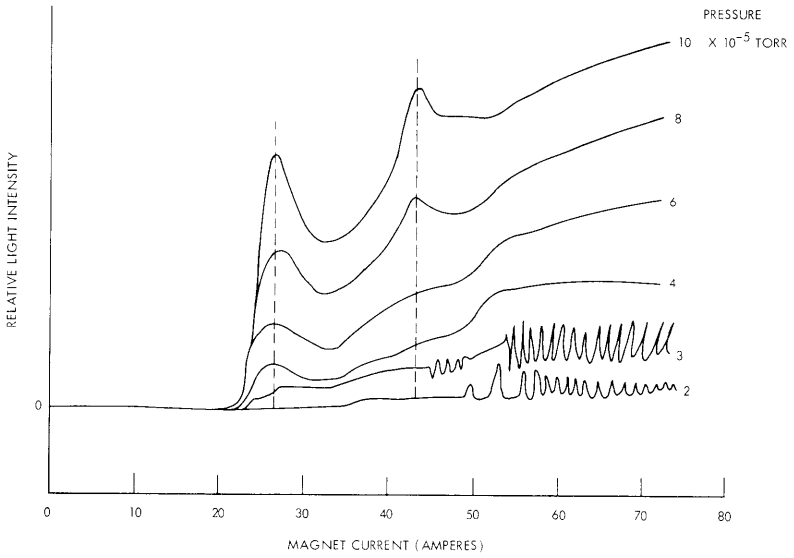


Fig. IX-12. Light versus B for various pressures.

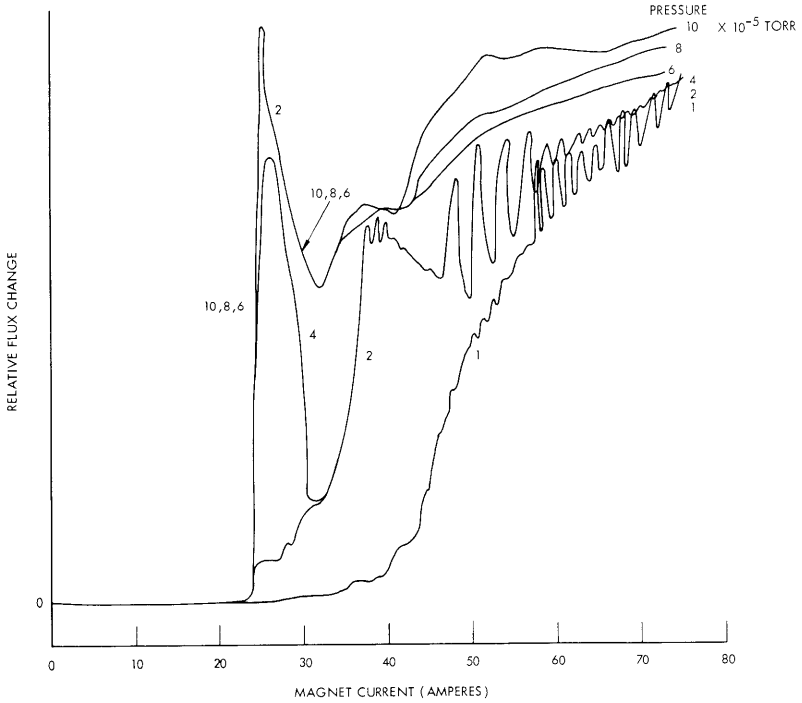


Fig. IX-13. Diamagnetic signal for the intermediate-pressure range.

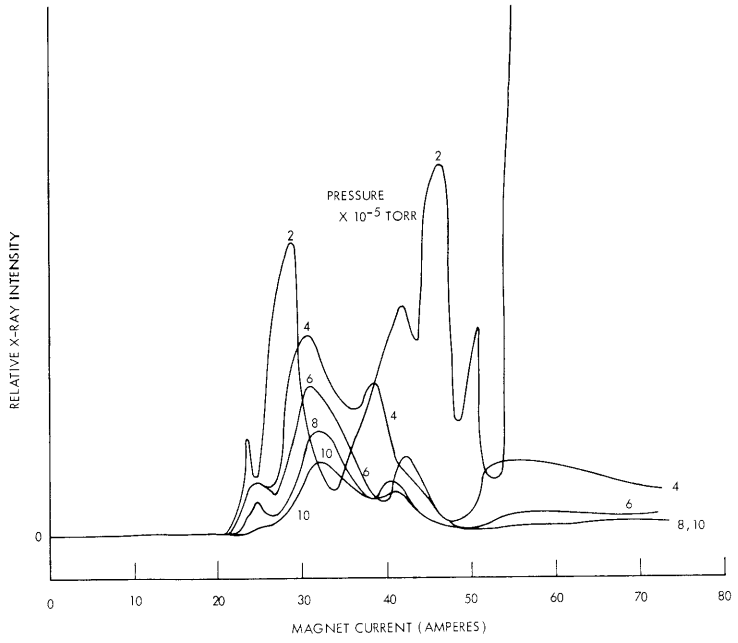


Fig. IX-14. X-ray intensity as a function of magnet current for various pressures in the intermediate-pressure range.

shape in the low-pressure regime. That is, the light continues to increase after the end of the microwave pulse. The maximum light intensity occurs approximately 5 μsec after the end of the microwave pulse. The light then decays until the next pulse occurs. The light-decay time constant in this range is given by the empirical relation $t = 5 \times 10^{-9}/p$, where p is in torr.

(ii) Diamagnetic Signal

Figure IX-13 is a graph of the relative diamagnetic signal strength as a function of the magnet current for various pressures. The interesting feature of these curves is their insensitivity to pressure changes. This is especially true at the breakdown point of 27 amps of magnet current. This indicates that the stored energy in the plasma is nearly constant in this range.

(iii) X-rays

Figure IX-14 is a graph of the x-ray intensity, as observed by using a sodium iodide scintillator, as a function of the magnetic field for the various pressures indicated. Here, one sees the rapid fall-off of x-ray intensity with increasing pressure. It is interesting to note that for the curves at 4, 6, 8, and $10 \times 10^{-5}$ torr the product of the x-ray intensity at the first peak and the pressure is very nearly constant.

c. High-Pressure Range

The high-pressure range begins at approximately $2 \times 10^{-4}$ torr and extends above $10^{-3}$ torr, which is the greatest pressure that has been investigated.

(i) Light

Figure IX-15 is a graph of the integrated light intensity as a function of pressure for various magnet currents. The only conclusion that could be drawn from these curves is that the light increases approximately linearly with pressure and that the transition from the intermediate range occurs at a pressure of $1.5 \times 10^{-4}$ torr.

Light as a function of magnet current is given in Fig. IX-16. One can see the maxima in light intensity at 27 amps and 46 amps which were also present in the intermediate-pressure range. Here, however, we see that breakdown occurs at lower magnet currents for the higher neutral-gas pressures.

The time dependence of the light pulse in this pressure range is different from that of the lower pressure ranges. The maximum of the light pulse coincides with the end of the microwave pulse – the light begins to decay immediately. The initial decay rate is considerably larger that its value a few microseconds later. At lower pressures the light continues to rise after the end of the microwave pulse for a few microseconds.

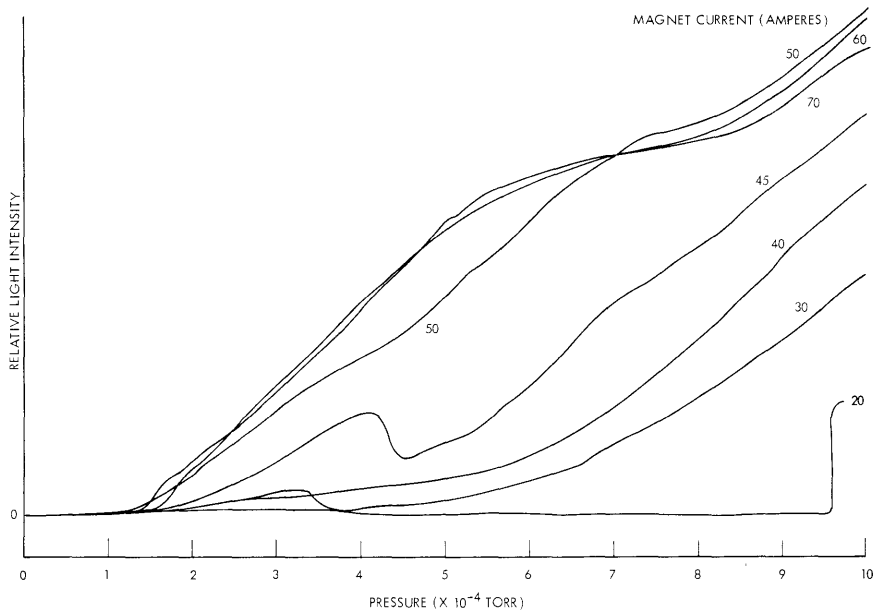


Fig. IX-15. Relative light intensity as a function of pressure for parametric magnetic fields.

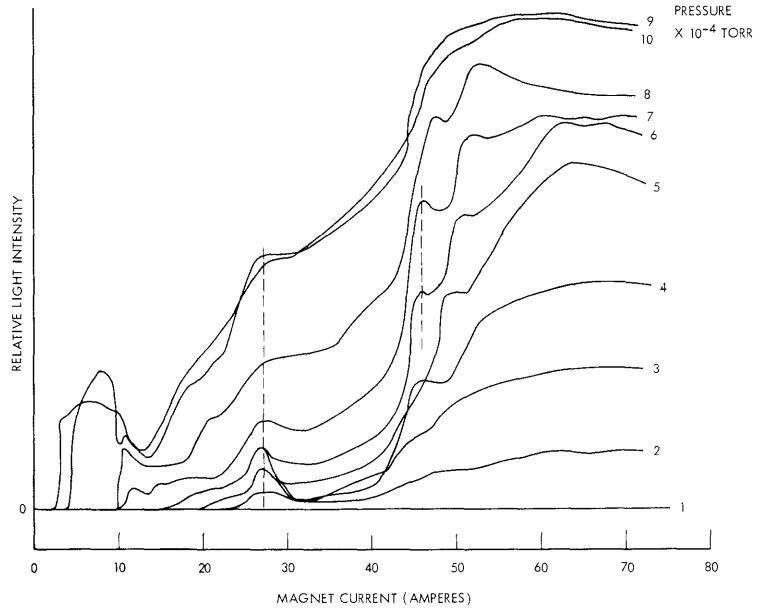


Fig. IX-16. Light versus magnetic field for parametric pressure.

(ii) Diamagnetic Signal

The diamagnetic signal as a function of the magnetic field is shown in Fig. IX-17 for the high-pressure region. The curve taken at a pressure of $2 \times 10^{-4}$ torr belongs in the intermediate-pressure range. Of particular interest in these curves is the fact that the sharp maximum at a magnet current of 26 amps does not exist in the high-pressure ranges. Also, the diamagnetic signal decreases with pressure, although in the intermediate range it increases with pressure. This indicates that the electron density is increasing with pressure and shielding the plasma from the microwave fields in the higher pressure range. The behavior of the light and the diamagnetic signals indicates that the electron gas on the average is much cooler than at the lower pressures. Therefore, it appears that future experiments will be mostly concerned with the lower pressure ranges.

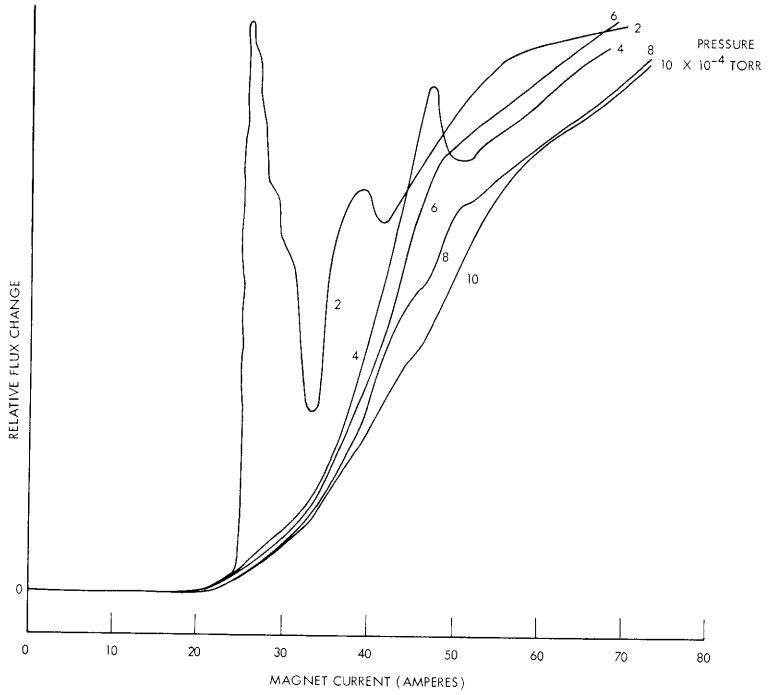


Fig. IX-17. Diamagnetic signal for the high-pressure range.

(iii) X-rays

In the high-pressure range the average x-ray intensity is very small. The ratio of the x-ray intensities during and after the microwave pulse is much smaller than at lower pressures and is approximately 5 or 10. Thus most of the x radiation occurs between the pulses.

T. J. Fessenden

References

1. G. Fiocco and L. D. Smullin, Electron-cyclotron plasma heating, Quarterly Progress Report No. 69, Research Laboratory of Electronics, M. I. T., April 15, 1963, pp. 63-65.

2. W. W. Ard, M. C. Becker, R. A. Dandl, H. O. Eason, A. C. England, R. J. Kerr, Thermonuclear Division Semiannual Progress Reports: ORNL 3472, April 30, 1963, Section 3.1; ORNL 3392, October 31, 1962, Section 3.1; ORNL 3315, April 30, 1962, Section 3.1; ORNL 3239, October 31, 1961, Section 3.1; ORNL 3104, January 31, 1961, Section 3.1.

## D. WAVE PROPAGATION IN HOT-ELECTRON PLASMAS

### 1. Introduction

The observation of low-frequency ($\sim\omega_{pi}$) oscillations in a beam-plasma discharge has stimulated the theoretical study of hot-electron plasma waveguides. An initial approach was made by Briggs and Bers.[1-3] They made use of the quasi-static approximation and the assumption that the thermal velocities are much larger than the beam velocity. The thermal motion of the electrons was assumed to have only a longitudinal component and was introduced into Maxwell's equations by using the Boltzmann transport equations. It is our intent to extend their work, in order to obtain more rigorous and general solutions of the hot-electron plasma problem.

### 2. Longitudinal Waves in an Infinite Plasma

In order to make a comparison between the transport equations and kinetic theory in their ability to describe a hot-electron plasma, longitudinal waves are being studied. An infinite plasma with cold ions and hot electrons is being investigated in three ways and the results will be compared. The three approaches involve:

#### a. Transport Equations

The ions are assumed to be cold and described by a delta-function at zero velocity. The electrons are assumed to be characterized by a double humped distribution $f_e$, symmetric about zero velocity. The drift velocity associated with the humps is $u_o$, and the spread is described by $v_T$ (Fig. IX-18).

The following dispersion equation was obtained for longitudinal plane waves.

$$0 = 1 - \frac{\omega_{pi}^2}{\omega^2} - \frac{\omega_{pe}^2}{2}\left[\frac{1}{(\omega-ku_o)^2 - k^2v_T^2} + \frac{1}{(\omega+ku_o)^2 - k^2v_T^2}\right]$$

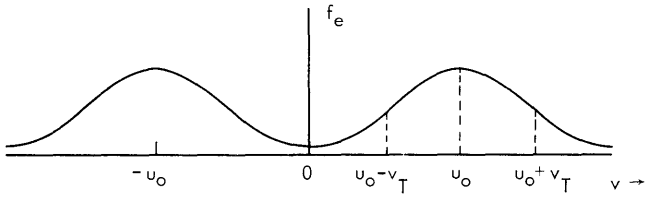


Fig. IX-18. Distribution used in transport equations.

b. Resonance Curve Distribution

The ion velocity distribution is assumed to be a delta-function at zero velocity. The electrons are described by a double humped resonance distribution (see Fig. IX-19). A dispersion relation was obtained by using kinetic theory and is

$$0 = 1 - \frac{\omega_{pi}^2}{\omega^2} + \frac{\omega_{pe}^2}{2}\left[\frac{1}{(i\omega - iku_o + kv_T)^2} + \frac{1}{(i\omega + iku_o + kv_T)^2}\right].$$

$$f_e = \frac{\frac{\alpha}{2\pi^2}}{[(v+u_o)^2+v_T^2]^2} + \frac{\frac{\alpha}{2\pi^2}}{[(v-u_o)^2+v_T^2]^2}$$

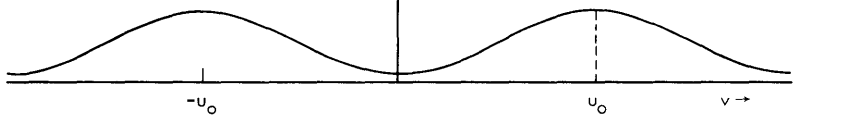


Fig. IX-19. Resonance distribution.

c. Square Distribution

Kinetic theory was used with a symmetric, double-square, distribution for electrons (see Fig. IX-20). As before, the ions were described by a delta function at zero velocity. The resulting dispersion relation is the same as that obtained from transport theory,

$$0 = 1 - \frac{\omega_{pi}^2}{\omega^2} - \frac{\omega_{pe}^2}{2}\left[\frac{1}{(\omega - ku_o)^2 - \frac{k^2v_T^2}{4}} + \frac{1}{(\omega + ku_o)^2 - \frac{k^2v_T^2}{4}}\right].$$

All the dispersion equations are sixth order in $\omega$ and fourth order in k. The dispersion curves ($\omega$-k) are being evaluated by the IBM 7090 computer, and the results

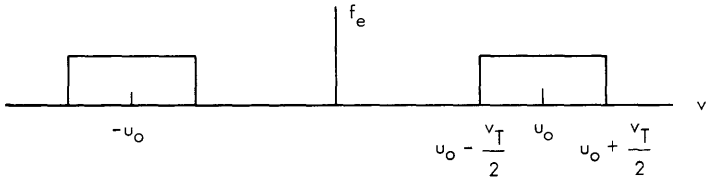


Fig. IX-20. Square distribution.

will be presented as plots of complex $\omega$ vs real k.

3. Hot-Electron Plasma Waveguides

The key to the dispersion relations for a finite plasma appears to be the dielectric tensor K defined as

$$\nabla \times \overline{H} = j\omega\epsilon_o \overline{E} + \overline{J} = j\omega\epsilon_o \overline{\overline{K}} \cdot \overline{E}.$$

The current density $\overline{J}$ is, in general, a function of the electric and magnetic field. Expressing $\overline{J}$ entirely in terms of $\overline{E}$ results in the $\overline{\overline{K}}$ tensor becoming an operator. For a finite plasma this tensor must be general enough to allow for the necessary transverse variation required to satisfy the boundary conditions.

Theoretical work has been started on the description of a waveguide filled with a cold-ion, hot-electron plasma. The random energy of the electrons is restricted to the longitudinal direction. Transverse AC and longitudinal DC magnetic fields are included. The electrons are described by an infinite number of streams in the manner described by Serafim.[4] The $\overline{\overline{K}}$ tensor below has been obtained by extending these summations to integrals.

$$\overline{\overline{K}} = \begin{bmatrix} K_{11} & K_{12} & K_{13} \\ K_{21} & K_{22} & K_{23} \\ K_{31} & K_{32} & K_{33} \end{bmatrix}$$

In cylindrical coordinates, with $\partial/\partial\theta = 0$.

$$K_{11} = 1 + \frac{\omega_p^2}{\omega^2} \int \frac{\omega_d f(v_o)}{\omega_b^2 - \omega_d^2} dv_o$$

$$K_{12} = -j \frac{\omega_b \omega_p^2}{\omega^2} \int \frac{\omega_d f(v_o)}{\omega_b^2 - \omega_d^2} dv_o$$

$$K_{13} = j \frac{\omega_p^2}{\omega^2} \frac{\partial}{\partial r} \int \frac{\omega_d v_o f(v_o)}{\omega_b^2 - \omega_d^2} dv_o$$

$$K_{21} = K_{12}^*$$

$$K_{22} = K_{11}$$

$$K_{23} = - \frac{\omega_p^2 \omega_b}{\omega^2} \frac{\partial}{\partial r} \int \frac{v_o f(v_o)}{\omega_b^2 - \omega_d^2} dv_o$$

$$K_{31} = j \frac{\omega_p^2}{\omega^2} \int \frac{\omega_d v_o f(v_o)}{\omega_b^2 - \omega_d^2} dv_o \frac{1}{r} \frac{\partial}{\partial r} r$$

$$K_{32} = \frac{\omega_p^2 \omega_b}{\omega^2} \int \frac{v_o f(v_o)}{\omega_b^2 - \omega_d^2} dv_o \frac{1}{r} \frac{\partial}{\partial r} r$$

$$K_{33} = 1 - \int \frac{\omega_p^2}{\omega_d^2} f(v_o) dv_o - \int \frac{\omega_p^2}{\omega^2} \frac{v_o^2 f(v_o)}{\omega_b^2 - \omega_d^2} dv_o \frac{1}{r} \frac{\partial}{\partial r} r \frac{\partial}{\partial r},$$

where

$\omega_d = \omega - kv_o$ n = particle density

$\omega_p^2 = \frac{q^2 n}{\epsilon_o m}$ q/m = charge to mass ratio

At the present time, the integrations are being carried out.

B. Kusse, M. T. Vlaardingerbroek

## References

1. R. J. Briggs and A. Bers, Electron-beam interactions with ions in a warm plasma, Quarterly Progress Report No. 69, Research Laboratory of Electronics, M.I.T., April 15, 1963, pp. 65-74.

2. R. J. Briggs and A. Bers, Interaction of electron beam with ions in a warm plasma of finite transverse dimension, Quarterly Progress Report No. 70, Research Laboratory of Electronics, M.I.T., July 15, 1963, pp. 129-133.

3. R. J. Briggs and A. Bers, Interaction of an electron beam with ions in a warm plasma of finite transverse dimension, Quarterly Progress Report No. 71, Research Laboratory of Electronics, M. I. T., October 15, 1963, pp. 131-137.

4. P. E. Serafim, Analysis of Electron Beam Plasma Systems, Ph. D. Thesis, Department of Electrical Engineering, M. I. T., February 1964.

## E. COMPUTER ANALYSIS AND DISPLAY OF WAVE INSTABILITIES

Techniques are being developed to use a digital computer and display device to facilitate applying the stability criteria derived by Bers and Briggs.[1]

The computer system is the IBM 7094 of Project MAC. A display console built by the Electronics System Laboratory, M. I. T., is connected to the Direct Data Connection of the IBM 7094 Data Channel.

The method of solution lies in first solving for the roots of the dispersion relation $D(\omega, k) = 0$ as a polynomial in $\omega$ with real values of k. The complex $\omega$-plane is then displayed to show the contours of the roots of complex $\omega$ as real k varies. $D(\omega, k) = 0$ is then solved as a polynomial in k with $\omega$ varying over values determined from the display of the $\omega$-plane. A display of the k-plane now shows the contours of the roots of k from which stability information can be determined.[1]

We have written a test program that solves for the roots of a dispersion relation whose solution was known previously. This program calculates the coefficients of the polynomial for a range of values of the variable (either $\omega$ or k), solves for the roots of the polynomial, and then displays these contours. At present, changing from the $\omega$-plane to the k-plane is accomplished by reading a second program into the computer. Provisions for dynamic interaction with the program are now being planned.

Photographs of the $\omega$-plane and k-plane displays for a particular example are shown in Fig. IX-21.

A. Bers, J. D. Mills

### References

1. A. Bers and R. J. Briggs, Criteria for determining absolute instabilities and distinguishing between amplifying and evanescent waves, Quarterly Progress Report No. 71, Research Laboratory of Electronics, M. I. T., October 15, 1963, pp. 122-131.

[See next page for Fig. IX-21.]

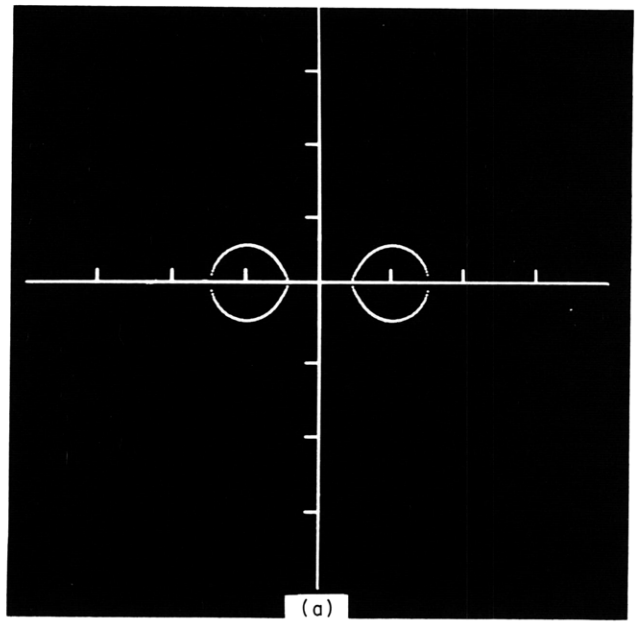


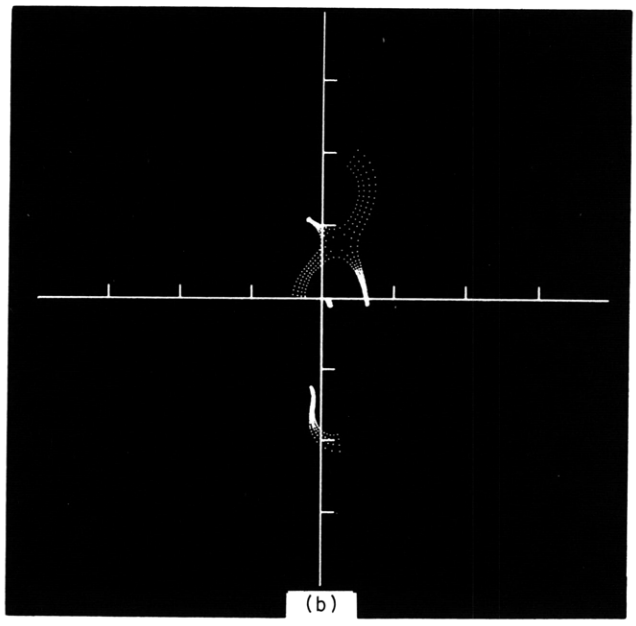


Fig. IX-21. (a) Complex ω-plane ($\omega_i$ vs $\omega_r$), showing contours of the real k axis. The L contour is taken just below these contours.[1] (b) Complex k-plane ($k_i$ vs $k_r$), showing loci of the roots of $D(\omega, k) = 0$ for values of ω varying from the L contours to the real ω axis, for four values of $\omega_r$.

## F. FUSION REACTOR BLANKET EXPERIMENT

### 1. Tritium Gas Target System

The operation of the tritium gas target that was designed to produce 14-mev neutrons by the $H^3(d,n)He^4$ reaction to bombard the fusion reactor blanket mock-up at the positive-ion facility of the Air Force Cambridge Research Laboratory, Bedford, Massachusetts, is described in this report. The construction of the gas target itself has been described earlier.[1]

#### a. Collimation System

The gas target holder is connected to a collimation system (see Fig. IX-22) and consists of (i) an aperture assembly with a 0.25-inch I.D. aperture and 0.5-inch I.D. baffle

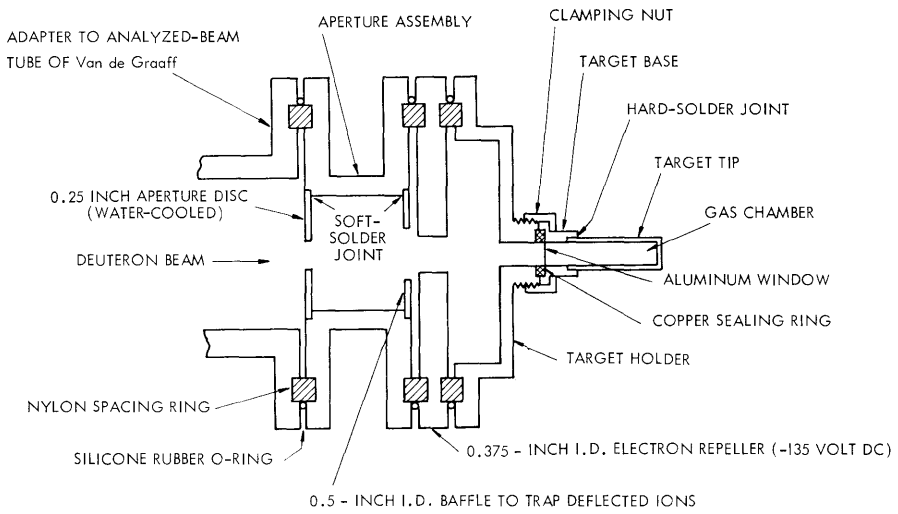


Fig. IX-22. Collimation system for gas target assembly. Aperture assembly, electron repeller, and target holder are held together by iron bolts covered with teflon tubing; use of fiber washers makes these joints electrically insulating. Water-cooling of 0.25-inch I.D. aperture disc and target holder is not shown.

to trap the deuterons that are deflected by large angles upon collision with the edge of the aperture, and (ii) an electron repeller with a 0.375-inch I.D. opening that is maintained at -135 volts to prevent the secondary electrons, which are emitted when deuterons strike the aperture and target, from confusing beam-current measurements. The aperture disc and the target holder are water-cooled. The components are positioned by nylon spacing rings, sealed by silicone rubber O-rings, and fastened by screws that are protected with teflon tubing and fiber washers to keep the joints electrically insulating. The assembly was attached to the analyzed beam tube of the 1-3 mev Van de Graaff

accelerator at the Air Force Cambridge Research Laboratory. Since the end of the tube was insulated from ground, the connection between the aperture assembly and the tube was not insulating.

The currents flowing from the aperture assembly, the electron repeller, and the target were monitored during the runs. The current from the electron repeller was zero. The target current measured the intensity of the deuteron beam, and the aperture current measured the focus and alignment of the beam. For a well-focused and correctly aligned beam of 3 μa on the target, the aperture current was <0.5 μa.

b. Uranium Reservoirs

The tritium for the gas target was obtained from uranium tritide in stainless-steel reservoirs, one of which is shown in Fig. IX-23. The system is similar to that described by Johnson and Banta.[2] The tritium was released by heating the reservoir to 410°C. For this purpose, a nichome heating wire was threaded on a boron nitride cylinder that could slip on the reservoir; a larger boron nitride cylinder covered the assembly. Stainless-steel snap rings held the heater in place. The temperature was measured by an iron-constantan thermocouple that was spot-welded to the bottom of the reservoir. The reservoir was sealed inside a water-cooled protective can to trap any tritium that might diffuse through the walls of the reservoir during the heating cycle.

The reservoir was constructed by welding a plug to the bottom of a stainless-steel tube 4 inches long, 0.25 inch I.D., and 0.375 inch O.D. The oxide layer was removed from 5-7 grams of depleted uranium foil scrap by momentarily immersing the foil in concentrated nitric acid, then rinsing, first in distilled water and finally in acetone. The air-dried foil was minced into the reservoir; the volume above the uranium was packed with glass wool, and the tube was welded to the stainless-steel feed tube (0.375 inch O.D., flared to 0.25 inch at the point of the weld) which led through the lid of the protective can (where it was fastened by a soft-solder joint). The other end of the feed tube was soft-soldered to a Hoke bellows valve (either No. 482 or A431). Johnson and Banta recommend a 0.125 inch O.D. feed tube butt-welded to a 0.25 inch O.D. plug, but we found that the butt weld leaked. Helium was flowed in through the furnace valve before heliarc welding to avoid igniting the uranium during the welding process. During the weld the reservoir tube was cooled by a wet cloth. Care had to be taken during the final stages of the welding that the heated gases inside the reservoir did not cause a pressure build-up and a blow-through in the weld. After the reservoir had been welded onto the lid assembly, the whole assembly was helium-leak tested before the thermocouple and heater connections were spot-welded into place.

The reservoir assembly was then connected to a manifold and pumped to ~1μ with the reservoir temperature at 410°C. Afterwards the reservoir was cooled to approximately 200°C and hydrogen was let into the system. After a short delay caused by

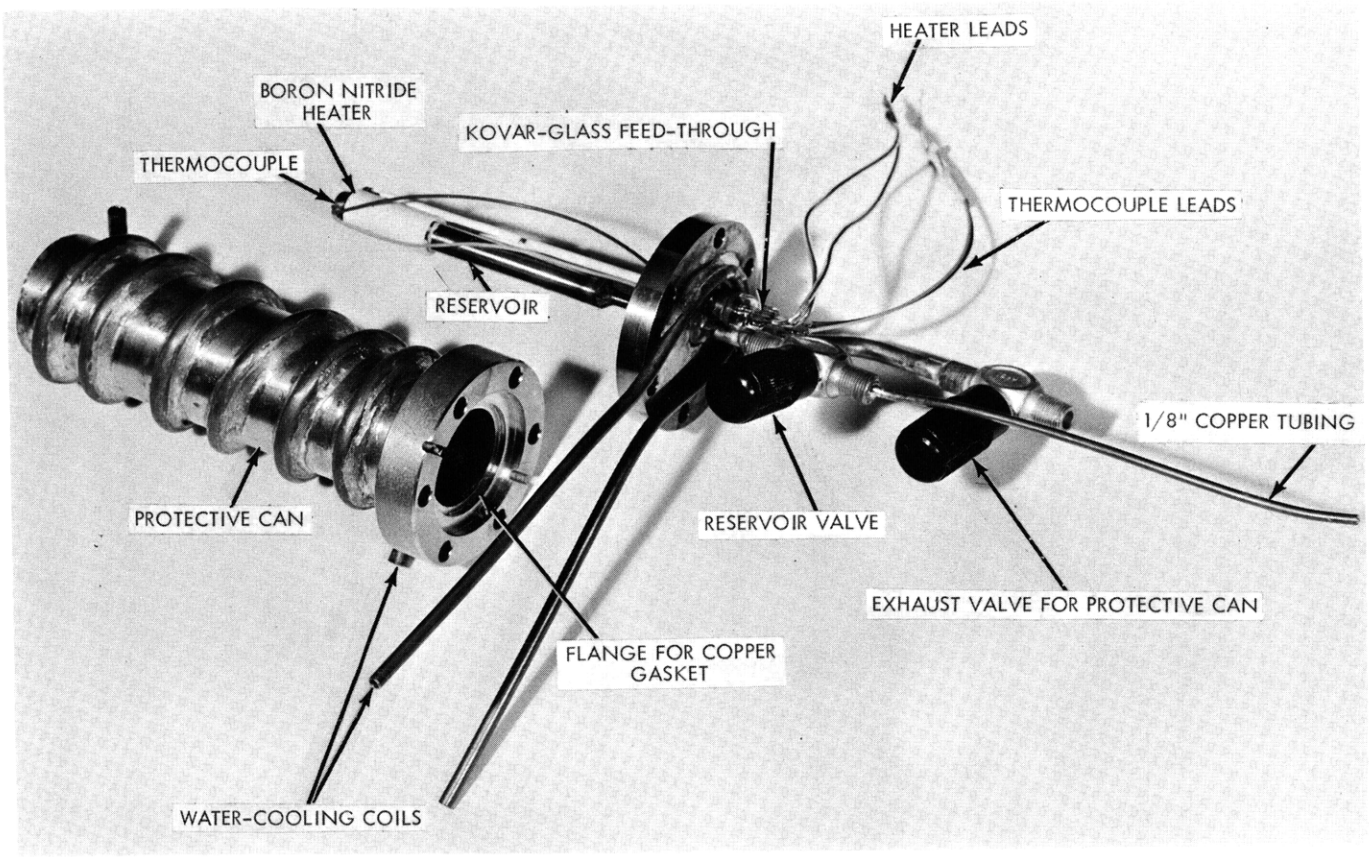


Fig. IX-23. Uranium tritide reservoir and protective can.

hydrogen diffusion through the surface oxide on the uranium, up to 1 liter-atmosphere of hydrogen was taken up within 30 minutes. After the hydriding reaction had ceased, the furnace was heated to 410°C and the hydrogen was pumped off to ~1 μ. This cycle was repeated several times to ensure activation of all of the uranium in the reservoir. If all of the uranium had been packed below the level of the heater, a system volume of hydrogen let in at 1 atm could be driven off at 1 atm by raising the reservoir temperature to 410°C — even in the presence of excess uranium. The excess uranium was necessary so that small amounts of air which would inevitably leak into the reservoir through the valve seat during transfer operations could be combined with the uranium (as a uranium nitride and uranium oxide) without impairing the effectiveness of the reservoir.

For transportation purposes the uranium reservoir in the protective can was placed in a helium atmosphere in a container whose lid was sealed with an O-ring. This container was, in turn, placed in a "2R" container that consisted of a cast-iron pipe with end caps.

c. Gas-Handling System

After the reservoir had been filled with 30 curies of tritium at the New England Nuclear Corporation in Boston, it was transported to AFCRL and connected to the gas-handling system shown schematically in Fig. IX-24, which consisted of an inner system

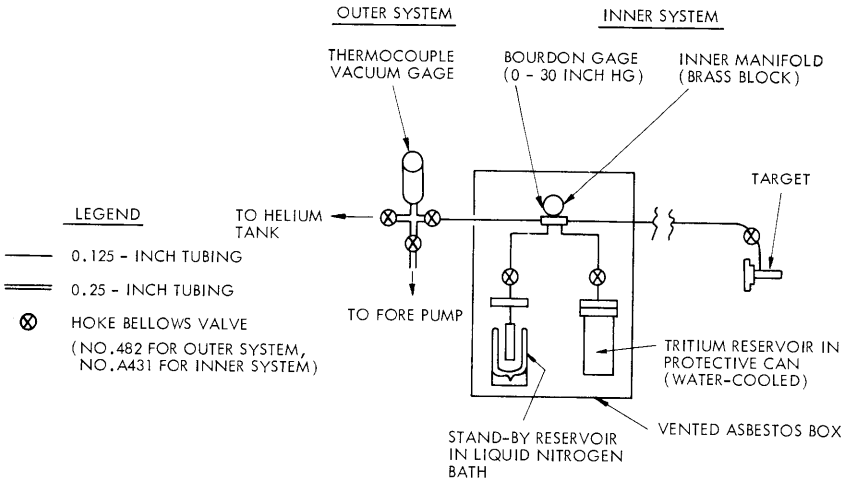


Fig. IX-24. Gas-handling system at the Air Force Cambridge Research Laboratory.

made of 0.125-inch copper tubing, a Bourdon gauge (0-30 inch Hg), the reservoir, a stand-by reservoir, and the gas target; and an outer system that contained a thermocouple vacuum gauge for routine leak checking and measuring the final take-up of tritium into the reservoir, and connections to a helium line for leak testing and to a forepump.

The stand-by reservoir was included in the system in case it became necessary to remove the tritium from the system while the tritium reservoir was still hot.

To reduce tritium contamination of the air in the target room, the asbestos box that contained the reservoirs and the forepumps for the tritium handling system and the accelerator were exhausted from a point 50 ft above the ground outside the building.

d. Safety Precautions

The work with the tritium required an ammendment to the AEC by-product material license held by M.I.T. In order to obtain this ammendment a comprehensive study[3] of the hazards involved was made with the cooperation of the Radiation Protection Committee of M.I.T. and the Wing Radiological Hazards Committee at AFCRL, and appropriate safety precautions were developed. Of chief concern were the possible release of all or some of the tritium into the atmosphere, and the contamination of personnel who operated the tritium system or who worked in the building.

A particular source of tritium release was the possible failure of the aluminum target windows. Extensive tests showed that while the window apparently would operate indefinitely (more than 12 hours) with a defocused beam of 6-7 μa, it would break within a minute at approximately 8 μa. Here a defocused beam is defined as one for which the target current and aperture current are equal. To guard against an accidental increase in current on the target window, a gate valve in the beam tube was closed automatically when the target current exceeded 7 μa. The gate valve was also closed automatically by a rise in pressure in the beam tube, or could be closed manually from the control room. A drop in the neutron flux, as monitored by a $BF_3$ detector, was also an indication of a leak.

Since there appeared to be a real possibility that all of the tritium might be released to the atmosphere in spite of the precautions, the total amount of tritium was kept to a minimum. As a result the tritium system volume had to be kept as small as possible. This led to a search for the smallest possible valves, gauges, and so forth, that could be used. The system described above appeared to be satisfactory.

e. Preliminary Operations

Before tritium operations began, the system was operated with deuterium. Measurements were made of the integral flux of neutrons from the $H^2(d, n)He^3$ reaction with 1 atm of deuterium in the target, by means of a calibrated $BF_3$ neutron detector. In Fig. IX-25 the experimental results, corrected for the energy degradation in the aluminum window, and the background neutrons (which were measured in a similar run with 1 atm He in the target), are compared with the calculated results of a theory[4] that was developed earlier. A sharply focused deuteron beam of 3 μa was used for these runs.

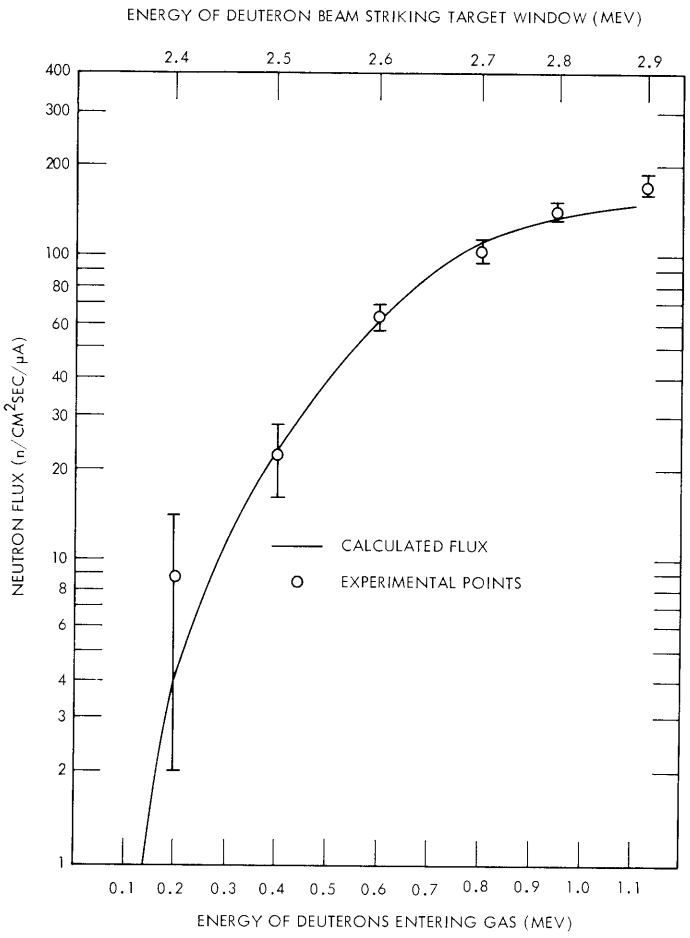


Fig. IX-25. Comparison of experimental and calculated values for neutron flux at a point 280 cm from a deuterium gas target at an angle 12.5° from the path of the deutron beam. Target contains 1 atm deuterium. Experimental points are corrected for background neuterons measured in a run in which target was filled with 1 atm He.

f. Operations with Tritium

After the tritium system shown in Fig. IX-24 was evacuated and checked, the valve connecting the inner and outer systems was closed, and the tritium reservoir was heated. Within approximately 20 minutes all of the tritium had been driven into the system, thereby raising the pressure to 0.6 atm. When the pressure had reached this (or a lower) limit, the target valve was closed, and the reservoir was allowed to cool, thereby reducing the pressure to less than 0.2 inch within a few minutes. The reservoir valve was closed and the run was begun. After the run the target and reservoir valves were opened to allow the gas in the target to be returned to the reservoir. Within a fewminutes the pressure was reduced to <0.2 inch Hg; within an hour the pressure could be reduced to <10 μ Hg. (In spite of these

splendid beginnings, the system did not operate satisfactorily.)

From the early runs it was concluded that between the times that the tritium reservoir was removed from the filling manifold and it was sealed in a helium atmosphere for transportation, air had entered the reservoir through the reservoir valve, which had not been properly closed, oxydizing some of the $T_2$ to $T_2O$. Overnight, between the time of installation of the reservoir and the first run, up to 10 curies of tritium were pumped out of the valve and exhausted up the stack. We reached the above-given conclusions on the basis of the following facts: (i) When the reservoir valve was opened for the run, it was found to be loosely closed. (ii) A careful calculation of the system volume revealed that less than 30 curies of tritium were being released when the reservoirs were heated – if all of the gas was assumed to be tritium. (iii) The neutron yield was low by a factor of 2. (iv) The shape of the curve of the neutron yield vs deuteron energy indicated the presence of a contaminant with a higher atomic number than 1. (v) The tritium contamination in the oil of the forepump was too high (8 mc/liter) after the first four runs to be explained as holdup of the few microcuries of $T_2$ which were evacuated from the system at the end of each run; if there were $T_2O$ in the gas, however, the high holdup was plausible.

At this point in the operations a leak developed at the joint at which the target line was soldered to the target valve – after the target had been filled and isolated from the system. The air leaked into the target to raise the pressure inside from 0.5 atm to ~1 atm. The two reservoirs were able to absorb all but a small amount of gas in the system (<5 mc had all of the gas been $T_2$); the remainder was exhausted through the forepump up the stack. It was necessary to dispose of both reservoirs. New ones were prepared under stricter specifications.

In the preparation of the second set of reservoirs, it became apparent that there was only a small difference between the tightness of the closure of the bellows valves which gave a satisfactory seal and that which would crack the bellows. Two alternatives were possible. (i) A larger and more sturdy commercial valve could be used, thereby increasing the volume of the system. This procedure would require a change in the AEC by-product material license. (ii) A custom-made valve in which the valve stem was supported by more than the bellows could be designed which would be sufficiently sturdy, and would still have the requisite small volume. The delays entailed by either alternative, coupled with the recent availability of Cockcroft-Walton accelerator (with which a solid tritium target can be used) at M.I.T., led to the decision to terminate gas target operations at AFCRL.

g. Tritium Contamination

During operations with tritium a program of wipe tests was conducted to control the spread of tritium contamination. The outside of the reservoir itself was highly

contaminated from its presence in a tritium hood during the filling operations (and possibly by tritium leaking through the reservoir valve). Immediately after the installation of the reservoir in the asbestos box, the whole inside of the box showed a tritium contamination of approximately 500 dpm for a 10-$cm^2$ wipe. Within a few days, however, the air flowing through the box (vented to the outside) had reduced contamination below measurable levels.

The only other major source of contamination was tritium adsorbed on the inner walls of the target chamber, which was released when the target windows were changed after each run as required by the AEC by-product material license. During window changes a portable hose connected to the ventilation system was held close to the target to entrap any tritium that might otherwise be released to breathing zones.

An air monitor[5] was used throughout all operations and indicated that at no time did the tritium concentration in the air exceed permissible levels ($2 \times 10^{-3}$ $\mu c/cm^3$). After 4 runs, urine samples were taken from all personnel in the building and analyzed for tritium content. In spite of the fact that disposable plastic gloves were worn by those handling potentially contaminated equipment, samples from the author and an assistant, who were involved in window changes, and from the technician who operated the accelerator, were 6.0, 4.0, and 0.6 $\mu c$/liter (uncertainty is ~0.2 $\mu c$/liter), which are less than the permissible level of 28 $\mu c$/liter. Samples from other personnel in the building, including those who supervised the window changes, showed no activity, indicating that contamination was spread by contact with contaminated equipment, rather than by inhalation of contaminated air.

2. Threshold Detectors

The following information is added to the previous report[1] of the series of threshold detectors which is being used to measure the neutron-energy spectra in the fusion reactor blanket mock-ups.

a. Uranium

The natural uranium foils have a background activity of ~$10^5$ cpm on the counting equipment used in these experiments. When the foils were irradiated for several hours at neutron fluxes of approximately $10^6$ n/$cm^2$ per sec, the activity was increased only by a few per cent. As a result the activity of the fission products that recoil into Mylar catchers will be counted, instead of the uranium foils themselves. Although the efficiency of the catcher technique is less, the counting statistics are much better.

b. Iron

The decay of $Mn^{56}$ from the $Mn^{55}(n,\gamma)$ reaction provides an undesirable background to the desired $Mn^{56}$ activity from the $Fe^{56}(n,p)$ reaction, even if there is only the

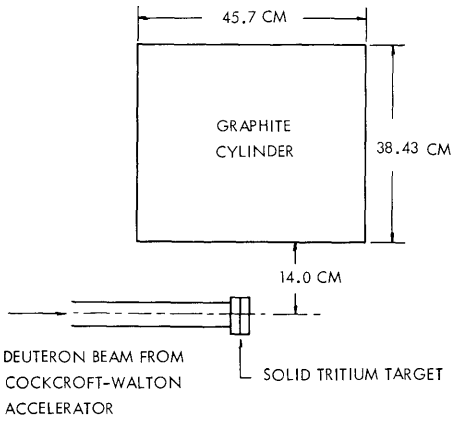


Fig. IX-26. Experimental arrangement.

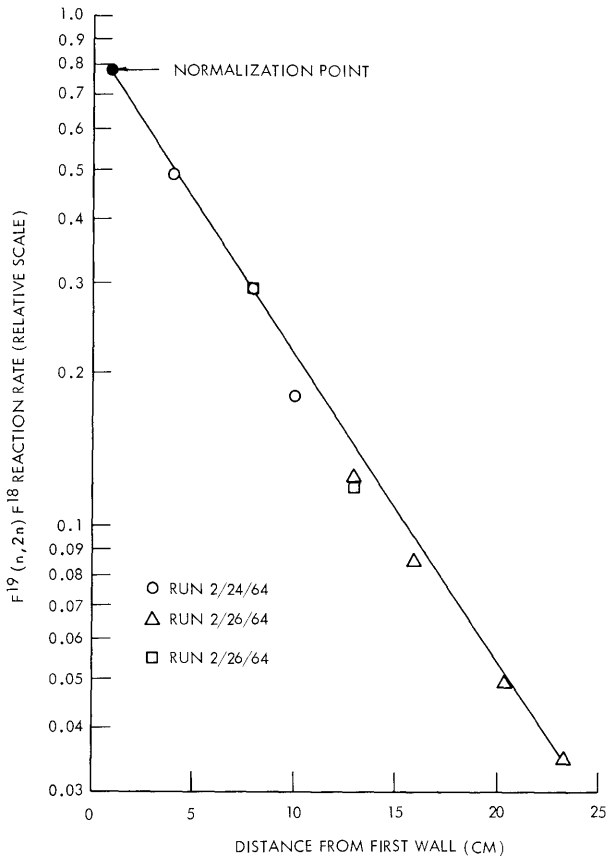


Fig. IX-27. Axial traverse in graphite blanket with teflon foils.

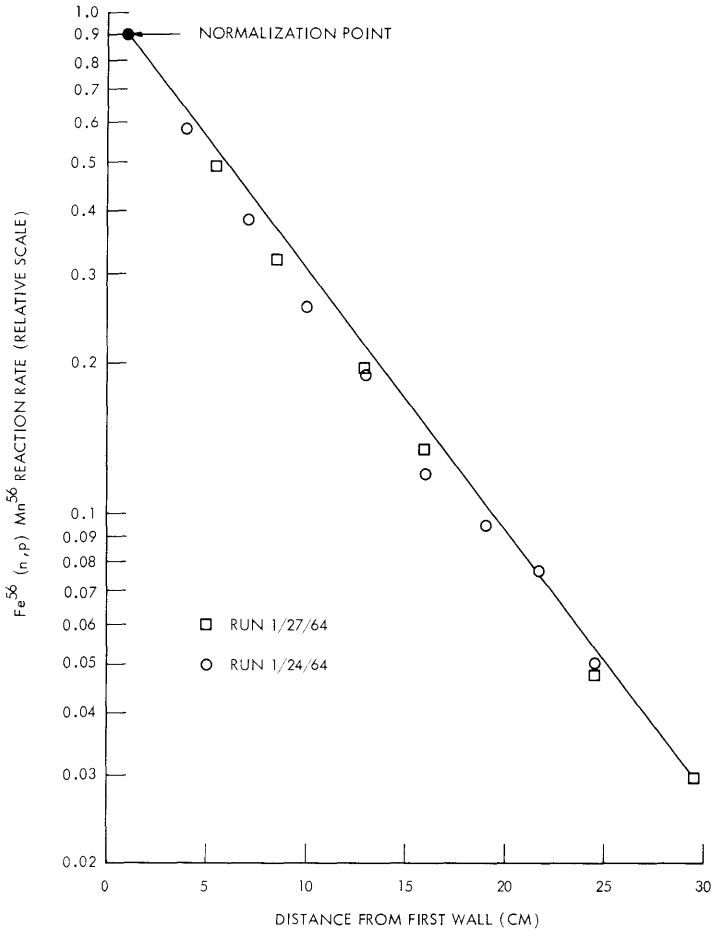


Fig. IX-28. Axial traverse in graphite blanket with iron foils.

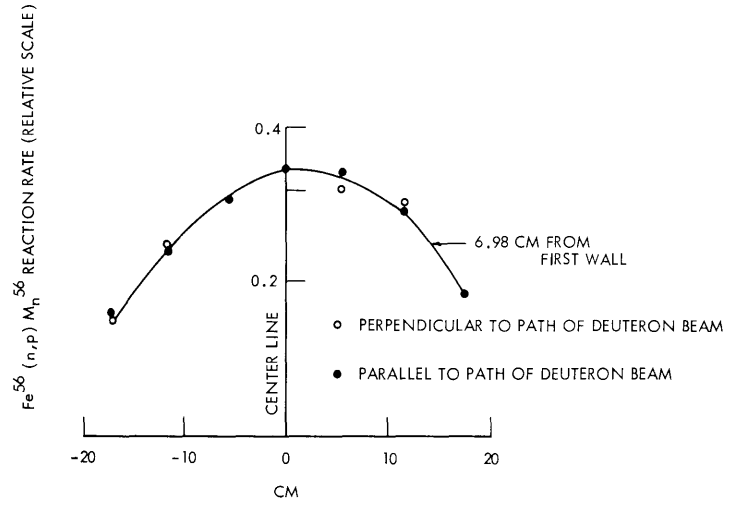


Fig. IX-29. Radial traverse in graphite blanket with iron foils. Normalization is the same as in Fig. IX-28.

0.5 per cent manganese present in commercially available high-purity iron. The iron foils used in these experiments were cut from a slug of iron with less than 10 ppm manganese which was obtained from the Department of Metallurgy, M.I.T.

c. Iodine

The foils used to measure the $I^{127}(n, 2n)I^{126}$ threshold reaction are made by compressing 2 grams of hexaiodobenzene powder into a mold at a pressure of 100 tons/in$^2$. The resulting pellets are of uniform size, nonhydroscopic, and reasonably sturdy.

3. Experimental Procedures

In the first series of runs axial and radial tranverses are being made in an all-graphite blanket mock-up with the threshold detectors to provide data for the development of a Monte Carlo code that is being written to provide a detailed description of the fusion blanket experiments. Details are shown in Fig. IX-26.

The mock-up is a graphite cylinder 45.7 cm in diameter and 1.48 cm thick, which consists of 26 graphite slabs. In the center of each slab is a circular depression 1.91 cm in diameter and 0.48 cm deep, which holds a cadmium pill box with the threshold detector(s). Two slabs have series of depressions along radii as well. Depressions that are not being used for foils in a given run are filled with a graphite button. The mock-up rests on an aluminum cart that can be rolled away from the target to remove the foils after the run. This procedure reduces exposure from the beta and gamma radiation that is induced in the target by the 14-mev neutrons.

The foils are counted by using an automatic sample changer that counts each foil for a preset number of counts and records the time required for the count. A computer program "SAMTAPE" has been written to reduce the data. The initial activities are computed by a modification of the Frantic program[6] which fits a sum of exponentials (with known half-lives) to the reduced data.

The axial and radial traverses that have been measured to date with iron and fluorine (teflon) foils are presented in Figs. IX-27 through IX-29.

P. S. Spangler

References

1. P. S. Spangler, Fusion reactor blanket experiment, Quarterly Progress Report No. 69, Research Laboratory of Electronics, M.I.T., April 15, 1963, pp. 81-88.

2. C. H. Johnson and H. E. Banta, Rev. Sci. Instr. 27, 132 (1956).

3. P. S. Spangler, Proposal for a 30-Curie Tritium Gas Target for Use with the 1-3 Mev Van de Graaf Accelerator at the Air Force Cambridge Research Laboratory, Bedford, Massachusetts (Unpublished, March 13, 1963).

4. P. S. Spangler, Fusion reactor blanket experiment: Neutron-energy spectrum from a tritium gas target, Quarterly Progress Report No. 71, Research Laboratory of Electronics, M.I.T., October 15, 1963, pp. 137-146.

5. Manufactured by Radiation Technology, Inc., Atlanta, Georgia.

6. P. C. Rogers, FRANTIC Program for Analysis of Exponential Growth and Decay Curves, Technical Report No. 76, Laboratory of Nuclear Science, M. I. T., June 1962.

## G. MODEL FOR ANOMALOUS RADIATION IN THOMSON-SCATTERING EXPERIMENTS*

The possibility of using intense monochromatic light beams to determine the velocity distribution of plasma electrons is being explored in many laboratories. This determination, based on measurement of the Doppler-broadened spectrum of a Thomson-scattered laser beam, appears to have sound theoretical footing, and the experimental techniques have been developed to a high degree of sophistication. Nonetheless, experiments[1,2] have been plagued by an unexpected broadband light signal from the plasma that often completely swamps the desired Thomson-scattered signal. We have developed a tentative explanation of this anomalous radiation and have completed an order-of-magnitude estimate of its importance.

### 1. Experimental Results

The experiments discussed below were performed near the core of a hollow-cathode discharge plasma generator.[3] The plasmas investigated (hydrogen, helium, and argon)

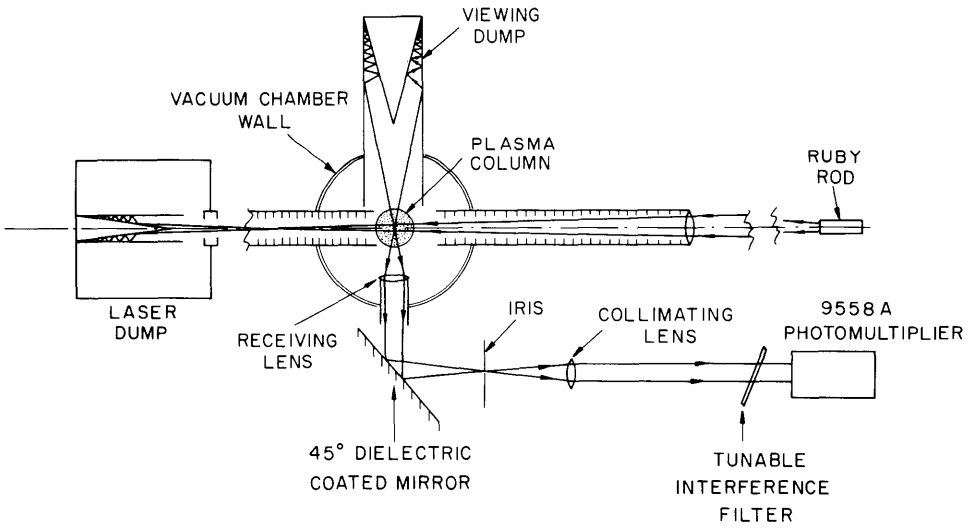


Fig. IX-30. Schematic diagram of Thomson-scattering experiment.

*This work was supported in part by the U. S. Atomic Energy Commission under Contract AF(30-1)-3285.

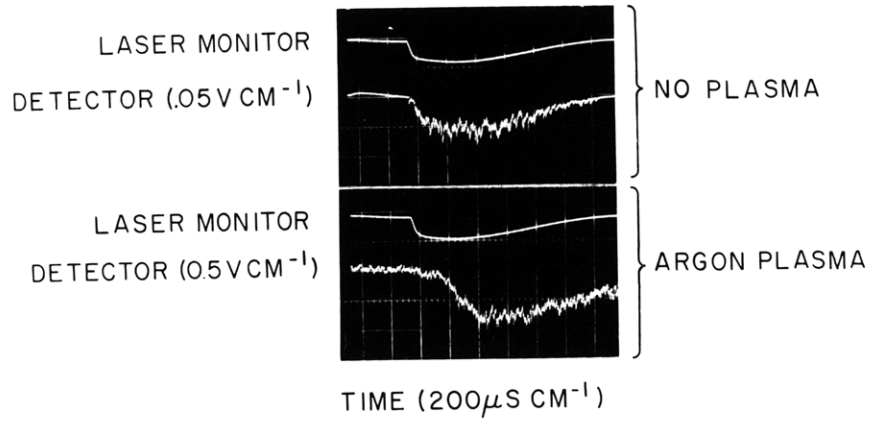


Fig. IX-31. Oscilloscope traces of input power (laser monitor) and output radiation (detector). The top trace shows the noise level caused by scattering of the input beam in the empty system.

had typical densities of $5 \times 10^{13}$ cm$^3$, electron temperatures of 1-5 ev, and background pressures of 1-10 microns. The light source was an $LN_2$ cooled ruby laser producing 20 joules of 6934 Å radiation in a 1.5-msec pulse. The detection system used a 5 Å bandpass dielectric film filter and an EMI 9558 photomultiplier. The experimental arrangement is shown in Fig. IX-30, and a detailed description has been given.[1]

The Thomson-scattered signal is expected to occur in time coincidence with the input laser signal and to have, at any given wavelength, its magnitude proportional to the instantaneous input power. The signal should appear, for a Maxwellian distribution of plasma electrons, as a Gaussian function of $\lambda - \lambda_o$ (where $\lambda_o$ = 6934 Å) with halfwidth of 50 Å for 5 ev electron temperature. The experimentally observed signal is delayed in time (see Fig. IX-31) and independent of wavelength over the 500 Å wide region explored. The signal magnitude is comparable to the calculated Thomson-scattered signal for small wavelength shift and far exceeds it for large values of wavelength shift. Furthermore, the anomalous signal is unpolarized, whereas the Doppler-shifted signal has the polarization of the input laser beam.

2. Source of Anomalous Signal

We suggest that the anomalous radiation observed is traceable to photoionization of excited neutral atoms in the plasma. The photoionization produces a local increase in ion and electron densities which, in turn, causes an increase in the recombination rate. Recombination from the continuum yields a broadband continuous spectrum with discontinuities at the "Balmer edges" appropriate to the ion under consideration. The time delay is caused by the time that is necessary for the incremental density increase to reach equilibrium between production by the laser pulse and diffusion away from the point of observation. We shall compute successively the photoionization cross section

for two cases, the incremental density increase, and the ratio of anomalous to Thomson-scattered radiation.

3. Computation of Photoionization Cross Section

The cross section for photoionization of a hydrogenic atom or ion from the state with principal quantum number j by a photon of frequency $\nu$ is given[4] by

$$\sigma(\nu, j) = g_j(32\pi^2 e^6 RZ^4)/3^{3/2}h^3\nu^3 j^5, \tag{1}$$

where R is the Rydberg constant and $g_j$ is the gaunt factor. For ruby laser frequency, $j \geq 3$ and $g_j \equiv 1.0$, this becomes

$$\sigma_{pj} = 3450 \times 10^{-18}/j^5 \text{ cm}^2. \tag{2}$$

The approximate cross sections given by Eq. 2 agree within 5 per cent with those given by the asymptotic expression derived by Burgess[5] and the numerical values tabulated by McDowell.[6]

The photoionization rate depends on the product of cross section and population for

Table IX-1. Tabulation of the lifetime against radiative decay, $\tau_r$, lifetime against excitation, $\tau_e$, and the lifetime against photoionization for some excited states of the hydrogen atom. The plasma and photon beam parameters are listed.

| j | $\tau_r$ (sec) | $\tau_e(j \rightarrow j+1)$ (sec) | $\tau_{pj}$ (sec) |
|---|---|---|---|
| 3 | $1.02 \times 10^{-8}$ | – | $2.9 \times 10^{-7}$ |
| 4 | $3.35 \times 10^{-8}$ | – | $1.2 \times 10^{-6}$ |
| 5 | $8.80 \times 10^{-8}$ | – | $3.8 \times 10^{-6}$ |
| – | – | – | – |
| 8 | | $3.6 \times 10^{-9}$ | $3.9 \times 10^{-5}$ |
| 9 | $[\tau_r \sim j^{4.5}]$ | $2.4 \times 10^{-9}$ | $7.1 \times 10^{-5}$ |
| 10 | | $1.8 \times 10^{-9}$ | $1.2 \times 10^{-4}$ |
| | | $\{n_e = 10^{13}/\text{cm}^3$, $T_e \sim 1$ ev$\}$ | {20 joules, $10^{-3}$ sec, 0.28 cm$^2$} |

each ionizable state ($j \geq 3$ for 6934 Å). In the absence of the leser pulse, the lifetime of the lower excited levels is determined by spontaneous decay to lower energy states. The numerical values of $\tau_r$, the lifetime against radiation, have been computed by Bethe and Salpeter[7] and are listed in Table IX-1.

The lifetimes of the upper ($n \geq 7$) excited levels are determined by collisional effects. This can be inferred from the theoretical and experimental result that in dense plasmas the upper states are in "Saha equilibrium" even though the plasma may be optically thin. Numerical values for the electron impact excitation cross sections are best evaluated by using Seaton's semi-empirical formulation, but for the upper levels these results are in the order of magnitude agreement with results based on the much simpler classical expression[8]

$$\sigma(i,j) = \pi e^4 E^{-1}\left[E_{ij}^{-1} - E^{-1}\right] \text{ cgs}, \tag{3}$$

for the cross section for transition between states of energy difference $E_{ij}$ caused by collision with an electron of energy E. The lifetime against excitation from state j to state j + 1, $\tau_e$, in a plasma density $10^{13}/\text{cm}^3$, where all electrons have 1 ev energy, computed from Eq. 3, is tabulated in Table IX-1. The actual lifetime must be much shorter than the tabulated values because the myriad of other possible reactions ($j \rightarrow j+2$, $j \rightarrow j-3$, etc.) have been ignored.

The lifetime against photoionization from state j is

$$\tau_{pj} = (n_p \sigma_{pj} c)^{-1}, \tag{4}$$

where $n_p$ is the photon density in the laser beam and c is the velocity of light. If we consider a $10^{-3}$-sec long square pulse of 20-joule total energy focussed to a beam diameter of 0.6 cm, we find

$$\tau_{pj} = 1.2 \times 10^{-9} j^5 \text{ sec}. \tag{5}$$

Equation 5 is also tabulated in Table IX-1. Notice that for any j, the lifetime against photoionization is much larger than either $\tau_r$ or $\tau_e$. The conclusion is that the laser pulse itself will not cause significant changes in the relative or absolute populations of the excited states. Thus, we can compute the photoionization rate on the basis of the population densities existing before the laser pulse.

4. Photoionization Cross Section

a. Maxwellian Electron Distribution

To simplify the following discussion, we consider one particular set of plasma properties. The values chosen are appropriate to the experiments described above. We take $n_e = n_i = 5 \times 10^{13}/\text{cm}^3$, $kT_e/e = 2.8$ ev, and fix the density of neutral atoms,

$n_1$, at $2 \times 10^{14}/cm^3$ (that is, a background pressure of 6 microns).

McWhirter and Hearn[9] have recently published the results of a theoretical study of the instantaneous population densities of excited levels of hydrogenlike ions in a plasma. They present an extensive tabulation of the coefficients $C_j$ and $D_j$ appearing in the expression

$$\frac{n_j}{n_j^s} = C_j + D\frac{n_1}{jn_1^s}, \tag{6}$$

where $n_j$ is the density of the $j^{th}$ excited level and $n_j^s$ is the Saha equilibrium population of the same level. Their results are in excellent agreement with the rather limited experimental data.[10]

For the plasma conditions assumed above, we find that the second term on the right-hand side of Eq. 6 is much larger than the first. This is a statement of the physical fact that the levels below $j \sim 10$ are populated by direct excitation from the ground state far more strongly then by cascade from the higher levels. This situation is common to many laboratory plasmas in which the electrons have a Maxwellian velocity distribution but the ground state is continually flooded by an influx of cold neutrals.

The macroscopic photoionization cross section, $\Sigma$, may be defined by

$$\sum = \sum_{j=3}^{\infty} n_j \sigma_{pj}. \tag{7}$$

We find, after application of Eqs. 2 and 6, that the first five terms of Eq. 7 yield

$$\sum \approx 2 \times 10^{-7}\ cm^{-1} \tag{8}$$

It is interesting to note that the j=3 contribution to the cross section exceeds that of the others ($j \geq 4$) more than an order of magnitude. Furthermore, for the given conditions, the numerical value of $\Sigma$ is almost directly proportional to the neutral density.

5. Streaming Electrons

Excitation from the ground state, the dominant process here, is a strong function of the high-energy tail of the electron distribution. We shall estimate the importance of a streaming high-energy group for the specific case of a helium plasma formed in the hollow-cathode discharge plasma source.

The steady-state density of an excited level is given by

$$n_j = n_1 \sigma_{1j}(v^*)\, n_e^* v^* \tau_j, \tag{9}$$

where $\sigma_{1j}$ is the cross section for excitation from the ground level to state j by electrons

of velocity $v^*$, and $n_e^*$ is the density of electrons with this velocity. We assume the presence of a single group of streaming electrons and consider only direct excitation and radiative decay. The core of the hallow-cathode discharge plasma is traversed by a high-energy group of streaming electrons with an estimated energy of 30 ev and a density of approximately $5 \times 10^{11}/cm^3$.[3]

For the $1s^2 \rightarrow 1s\,3p$ transition in neutral helium, Eq. 3 gives $\sigma_{13} \approx 2 \times 10^{-18}$ cm$^2$. Lees' experimental value for this cross section is $0.72 \times 10^{-18}$ cm$^2$.[11] We take $\sigma_{13} = 10^{-18}$ cm$^2$. The lifetime, $\tau_j$, of the 3p state is $11.5 \times 10^{-8}$ sec. Therefore, the macroscopic cross section resulting from the streaming group is

$$\sum' \approx 5 \times 10^{-8}\ \text{cm}^{-1}. \tag{10}$$

Thus, for a rather typical laboratory plasma, the contribution to the photoionization cross section by streaming electrons is comparable to that of the main body of the electron distribution. Note that the value of $\Sigma'$ also varies directly with the background pressure.

6. Density and Recombination Increments

The increment in plasma density at the point of observation is determined by the balance between the production and diffusion rates at the point of observation. Within the accuracy of the present computations, it is probably sufficient to assume that the excess plasma produced fills the entire length of the magnetic flux tube intersecting the observation region and that the lifetime, $\tau_L$, of an ion in this flux tube is that of an average plasma ion. The assumption of uniform density within the flux tube is justified by the arguments that the excess density perturbation should spread along field lines with a velocity near that of an ion sound wave and that the sound-wave transit time for the system is short compared to the build-up time of the anomalous radiation pulse. The second assumption is bolstered by the agreement between $\tau_L$ and the decay time of the radiation pulse observed in preliminary experiments. Thus, we have

$$\frac{dn_e'}{dt} = \frac{n_p c\, \Sigma}{\overline{L}_1} - \frac{n_e'}{\tau_L}, \tag{11}$$

where $n_e'$ is the increment in plasma density, $n_p c$ is the photon flux during the laser pulse ($2.4 \times 10^{23}/cm^2$ in the present case), the system length, $\overline{L}_1$, is 30 cm, and $\tau_L$ is $5 \times 10^{-3}$ sec. For the steady-state solution, this yields

$$n_e' = 1 \times 10^{12}/cm^3. \tag{12}$$

The increment in the volume recombination rate, W, is given by

$$\Delta W = 2\alpha(n_e, T_e)\, n_e n'_e \text{ cm}^{-3} \text{ sec}^{-1}, \tag{13}$$

where the recombination coefficient, $\alpha$, is a function of density and temperature because three-body recombination is the dominant process. For $\alpha(5 \times 10^{13}/\text{cm}^3, 2.8 \text{ ev}) = 10^{-12}$, we find[12,13]

$$\Delta W = 1 \times 10^{14}/\text{cm}^3 \text{ sec}. \tag{14}$$

7. Comparison of Radiation Intensities

The Thomson-scattering rate, $W_T(\lambda)$, for a Maxwellian distribution of free electrons at temperature T is

$$W_T(\lambda) = \frac{n_p c n_e \sigma_T}{\pi^{1/2} \lambda_T} e^{-(\lambda/\lambda_T)^2}, \tag{15}$$

where $\lambda$ is the wavelength shift, $n_e$ is the density of free electrons, $\sigma_T$ is the Thomson-scattering cross section, and for 90° scattering of radiation of wavelength $\lambda_o$

$$\lambda_T^2 = 8\lambda_o^2 kT/mc^2. \tag{16}$$

The scaling coefficient, $\lambda_T$, is the linear Doppler shift for a particle with 8 kT energy. For the parameters listed above,

$$W_T(\lambda) = 9.8 \times 10^{10}\, e^{-(\lambda/45.6)^2} \text{ photons/cm}^2 \text{ sec Å}. \tag{17}$$

The increment in recombination light per unit wavelength, $\Delta W(\lambda)$, is a number that is more difficult to estimate, but we shall use Seaton's value computed for recombination in tenuous plasmas[14] corrected by the ratio of collisional radiative to purely radiative recombination for the hollow-cathode discharge plasma. This process yields

$$\Delta W(\lambda_o) = \frac{2\gamma(\lambda_o)\, n_e n'_e}{\lambda_o}$$

$$= 1.5 \times 10^{10} \text{ photons/cm}^2 \text{ sec Å}. \tag{18}$$

The agreement between $W_T(\lambda)$, the volume emission rate of Thomson-scattered photons, and $\Delta W(\lambda_o)$, the volume increment in recombination photons near $\lambda_o$, is evidence that the mechanism proposed may, in truth, be the source of the anomalous signal.

Entirely apart from the assumptions made in the calculations above, there is another factor acting to increase the ratio of recombination to scattered signals. The rates above have been calculated for a unit volume of plasma, but the plasma volume actually

emitting increased recombination far exceeds the plasma volume traversed by the laser beam. The ratio of signals received must therefore be multiplied by the ratio of active observation volume to the volume traversed by the laser beam.

The mechanism proposed here should be most important in plasmas of relatively high electron temperature and low degree of ionization. A more sophisticated analysis of its relative importance as a function of plasma properties is under way. It should be noted that large anomalous signals do not obviate the use of Thomson-scattering diagnostics because the unpolarized recombination signal is inherently different from the polarized scattered radiation. The Doppler-shifted signal can be retrieved as the difference between the radiation intensities in the polarizations parallel and perpendicular to the input laser beam.

The increment in recombination light depends linearly on the background pressure in the plasma. Experiments now under construction should quite easily be able to determine its importance for the hollow-cathode discharge generated plasma.

L. M. Lidsky, D. J. Rose, E. Thompson

## References

1. E. Thompson and G. Fiocco, Quarterly Progress Report No. 69, Research Laboratory of Electronics, M.I.T., April 15, 1963, p. 74.

2. S. E. Schwarz, Proc. IEEE 51, 1362 (1963).

3. L. M. Lidsky, S. D. Rothleder, D. J. Rose, and S. Yashikawa, J. App. Phys. 33, 2490 (1962).

4. R. W. Ditchburn and V. Opik, Atomic and Molecular Processes, edited by D. R. Bates (Academic Press, Inc., New York, 1962), p. 86.

5. A. Burgess, M. N. Roy. Astron. Soc. 118, 447 (1958).

6. M. R. C. McDowell, ORNL-347, Semi-annual Progress Report for period ending April 30, 1963, p. 64.

7. H. Bethe and R. Salpeter, Handbuch der Physik, Vol. V, edited by S. Flügge (Springer-Verlag, Berlin, 1957), p. 352.

8. J. J. Thomson, Phil. Mag. 47, 337 (1924).

9. R. W. P. McWhirter and A. G. Hearn, Proc. Phys. Soc. (London) 82, pt. 5, 641 (1963).

10. E. Hinnov and J. G. Hirschberg, Phys. Rev. 125, 795 (1962).

11. J. H. Lees, Proc. Roy. Soc. (London) A123, 73 (1932).

12. D. R. Bates and A. E. Kingston, Nature 189, 652 (1961).

13. R. W. P. McWhirter, Nature 190, 902 (1961).

14. M. J. Seaton, Rep. Prog. Phys. 23, 313 (1960).

## H. FIELD CONFIGURATIONS IN THE STUFFED CUSP

"Minimum-B" confinement systems appear to offer the best hope of stable plasma confinement. As a preliminary step in the design of an experiment embodying this

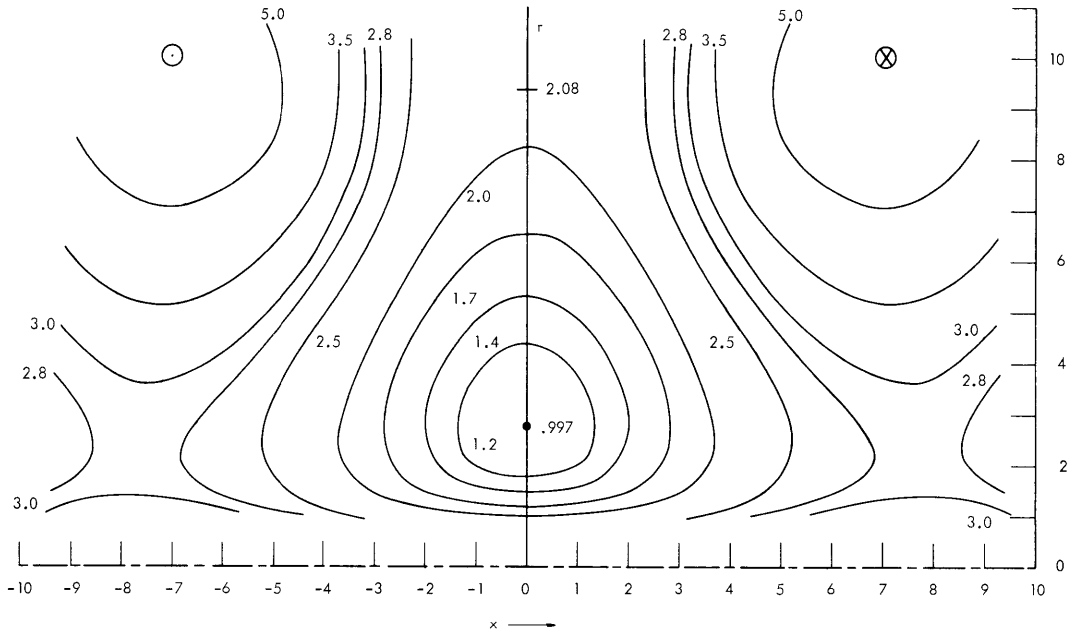


Fig. IX-32. Contours of constant $|\vec{B}|$ in a stuffed-cusp system. The coil separation is 1.4 × the coil radius. F, the ratio of central conductor to coil current, is 0.2. The scaling factor between $|\vec{B}|$ and current is $\mu/2\pi$, that is, B = $2 \times 10^{-3}$ gauss/ampere-turn for a 1.0-meter radius.

principle, we have been study ing field configurations in the stuffed cusp (a spindle cusp with the addition of a current-carrying conductor along the central axis). Figure IX-32, an early result of these studies, is a plot of the contours of constant $|\vec{B}|$ for a particular arrangement of coil spacing and coil/center conductor current ratios. The system shown offers an interesting combination of properties – good access, large containment volume, reasonable mirror ratio, and low current in the central conductor.

The easily accessible line cusp opens intriguing possibilities for nonadiabatic plasma injection. We are investigating the possibility of using a properly modified "Corkscrew."

L. M. Lidsky

### References

1. Yu. B. Gott et al., Nuclear Fusion Suppl. Pt. III, 1045 (1962).
2. J. B. Taylor, Phys. Fluids 6, 1592 (1963).

3. R. C. Wingerson, T. H. Dupree, and D. J. Rose, Charged-particle trapping and loss in a perturbed magnetic field (Phys. Fluids, in press).